JGR Solid Earth

RESEARCH ARTICLE
10.1029/2022JB025716

Key Points:

- Stochastic modeling can reproduce **M**9 ruptures with low dissimilarity to real events
- Including coupling into the stochastic method can have both positive or negative effect based on the "correctness" of the coupling model

Correspondence to:
D. T. Small,
dsmall2@uoregon.edu

Citation:
Small, D. T., & Melgar, D. (2023). Can stochastic slip rupture modeling produce realistic **M**9+ events? *Journal of Geophysical Research: Solid Earth*, *128*, e2022JB025716. https://doi.org/10.1029/2022JB025716

Received 30 SEP 2022
Accepted 8 MAR 2023

Author Contributions:
Conceptualization: David T. Small, Diego Melgar
Data curation: David T. Small
Formal analysis: David T. Small
Investigation: David T. Small
Methodology: David T. Small
Project Administration: Diego Melgar
Software: Diego Melgar
Supervision: Diego Melgar
Validation: David T. Small
Writing – original draft: David T. Small
Writing – review & editing: Diego Melgar

Can Stochastic Slip Rupture Modeling Produce Realistic M9+ Events?

David T. Small[1] and **Diego Melgar**[1]

[1]University of Oregon, Eugene, OR, USA

Abstract Stochastic slip rupture modeling is a computationally efficient, reduced-physics approximation that has the capability to create large numbers of unique ruptures based only on a few statistical assumptions. Yet one fundamental question pertaining to this approach is whether the slip distributions calculated in this way are "realistic." Rather, can stochastic modeling reproduce slip distributions that match what is seen in **M**9+ events recorded in instrumental time? We focus here on testing the ability of the von Karman ACF method for stochastic slip modeling to reproduce **M**9+ events. We start with the 2011 **M**9.1 Tohoku-Oki earthquake and tsunami where we test both a stochastic method with a homogeneous background mean model and a method where slip is informed by an additional interseismic coupling constraint. We test two coupling constraints with varying assumptions of either trench-locking or -creeping and assess their influence on the calculated ruptures. We quantify the dissimilarity between the 12,000 modeled ruptures and a slip inversion for the Tohoku earthquake. We also model tsunami inundation for over 300 ruptures and compare the results to an inundation survey along the eastern coastline of Japan. We conclude that stochastic slip modeling produces ruptures that can be considered "Tohoku-like," and inclusion of coupling can both positively and negatively influence the ability to create realistic ruptures. We then expand our study to show that for the 1960 **M**9.4–9.6 Chile, 1964 **M**9.2 Alaska, and 2004 **M**9.1–9.3 Sumatra events, stochastic slip modeling has the capability to produce ruptures that compare favorably to those events.

Plain Language Summary Stochastic slip rupture modeling is an effective and simple method for generating a unique number of earthquakes based on only a few statistical parameters. Although the parameters that define these synthetic ruptures are calculated from real earthquakes, the validity of the determined slip patterns for large magnitude ruptures is not completely certain. Here, we answer the question of can stochastic modeling reproduce slip distributions that match what is seen in **M**9+ events recorded in instrumental time? We start with the 2011 **M**9.1 Tohoku-Oki earthquake and tsunami where we test both a more traditional approach to stochastic modeling as well as an approach that utilizes a fault zone's pattern of geodetic coupling to inform slip. We quantify the dissimilarity of slip distribution between the ruptures and a Tohoku earthquake model. We also generate tsunami models for some ruptures and compare their results to an inundation survey following the Tohoku earthquake. We conclude that stochastic slip modeling can produce ruptures that can be considered "Tohoku-like." We then expand our study to and show that for the 1960 **M**9.4–9.6 Chile, 1964 **M**9.2 Alaska, and 2004 **M**9.1–9.3 Sumatra events, stochastic slip modeling has the capability to produce realistic ruptures.

1. Introduction

Unlike other rupture modeling techniques, stochastic slip modeling utilizes a reduced-physics approximation. Rather than solving for a fully dynamic rupture that includes fault zone characteristics like stress drop, material properties, and friction, it assumes that ruptures can be more simply described by only a few different statistical parameters inferred from observations of real earthquakes (Mai & Beroza, 2002). In this view, slip distributions are realizations of an underlying probability density function. The computational cost of determining ruptures for large magnitude events is reduced significantly, allowing for a greater quantity of unique events to be calculated in a short amount of time with modest resources. Studies that have shown to greatly benefit from use of stochastic models include earthquake early warning, where ruptures produced can be used to test existing algorithms (e.g., Ruhl et al., 2017), train advanced machine learning algorithms (e.g., Lin et al., 2021), as well as to seismic and tsunami hazard assessments where ruptures inform localized hazards (e.g., Graves et al., 2011; LeVeque et al., 2016; Small & Melgar, 2021).

In this work, we focus on the technique first introduced by Mai and Beroza (2002) where they determined that the best fitting autocorrelation function (ACF) that describes the stochastic nature of slip is the von Karman ACF (VK ACF). The approach has also been used by Lavallée & Archuleta, 2003, however, their procedures differ slightly on how they compute the power spectrums. This is not the only way to carry out stochastic rupture modeling. Herrero and Bernard (1994) first proposed the "k-square" spectral decay approach to generating synthetic finite fault models which assumes a fractal representation of slip. The k-square method has been used and modified throughout the years (e.g., Davies et al., 2015; Ruiz et al., 2007). The k-square and the VK ACF method differ predominantly on their assumptions of the necessary length scales across which slip correlates. The k-square method only requires a single characteristic source dimension, whereas the VK ACF additionally uses correlation lengths to describe the dominant slip asperities following the findings from Somerville et al. (1999). Some of these stochastic methods have been validated in some manner based on past ruptures and their ensuant tsunamis, however, the von Karman ACF method has not been tested for its applicability and ability in producing great earthquakes.

Indeed, as new earthquakes occur, there have been numerous efforts to validate the different scaling laws and statistical parameters underpinning these approaches (e.g., Goda et al., 2016; Melgar & Hayes, 2019). Previous studies that have attempted to validate the stochastic method have done so by comparing against the tsunami that results from actual ruptures, rather than by a comparison to the slip patterns themselves. For instance, Geist et al. (2007) tested the stochastic slip approach's ability to reproduce run-up observations consistent with the 2004 M9.2 Sumatra earthquake. In a similar approach, Davies et al. (2015) tested nine variations of a k-square approach to generating synthetic finite fault models and evaluated them by comparing the tsunami they produced to that obtained from slip inversions. Of these nine variations, the favored method was then used by Davies (2019) to test the stochastic tsunamis generated at DART buoy locations from 17 **M** > 7.8 global ruptures. Goda et al. (2015) and Mori et al. (2017) tested the sensitivity and variability of inundation from stochastic models. These were generated using a known slip inversion as a reference or "background" model. They also tested ruptures produced without knowledge of the slip model. Mori et al. (2017) determined that tsunami inundation was strongly influenced by the source model applied when calculating the synthetic ruptures.

Other previous works have been focused on testing the uncertainties and sensitivities of utilizing stochastic slip ruptures for probabilistic tsunami hazard assessment (PTHA, e.g., Murphy et al., 2016; Sepúlveda et al., 2019; Scala et al., 2020). Murphy et al. (2016) uses a modified stochastic slip approach that incorporates systematic ruptures features observed in dynamic models focused on the 2011 **M**9 Tohoku event. With these modified models, they calculate the probability of wave height exceedance along the Japan coast and compare these statistics with the observed wave heights from the actual tsunami.

Additionally, there have been proposals to incorporate more detailed geophysical knowledge while maintaining computational efficiency into stochastic slip models. Small and Melgar (2021) proposed a way to utilize interseismic coupling to inform slip distribution. In this method, the goal is to use a fault zone's coupling pattern as the "background" model to pre-condition stochastic slip distributions, so that the resultant hypothetical ruptures correlate to it and the calculated ruptures are potentially more representative of the specific region's earthquake potential. In this work we leverage that approach. For many recent large ruptures where coupling models existed prior to the event, a modest correlation between large coseismic slip patches and regions of high coupling ratio has been noted. This correlation is seen in Chile (Barnhart et al., 2016; Metois et al., 2013), Peru (Perfettini et al., 2010; Villegas-Lanza et al., 2016), Alaska (Li & Freymueller, 2018), and Japan (Loveless & Meade, 2015). By including coupling in the modeling process, we posit that ruptures may have a greater likelihood of being more realistic. Yet, we acknowledge that this correlation does not necessarily equate to causation. The presence of a highly coupled zones may not directly indicate the location of large slip propagation, creating uncertainty in the slip pattern predictive nature of coupling. For instance, some previous earthquakes have ruptured only a portion of the highly coupled zone (e.g., Konca et al., 2008; Moreno et al., 2010; Perfettini et al., 2010). Similarly, our lack of instrumentation offshore in the shallow-most portion of the subduction zones creates great uncertainty in coupling models (e.g., Lindsey et al., 2021; Wang & Trehu, 2016). So, the question of the validity of the ruptures generated using a coupling model as a pre-condition is important to answer.

So, in this work, we explore two basic research questions. (a) Can the von Karman ACF approach to stochastic slip rupture modeling reproduce slip distributions that match great (**M**9+) earthquakes recorded in instrumental time? (b) If interseismic coupling is included as a priori constraint, does this better reproduce large ruptures?

We use this study as a formal check for the application of stochastic slip modeling in calculating "realistic" large ruptures.

To answer these questions, we look at four different **M**9+ events: the 2011 Tohoku-Oki, Japan **M**9.0–9.1, 1960 Chile **M**9.2–9.4, 2004 Sumatra **M**9.1–9.3, and 1964 Alaska **M**9.2. We note that since reliable coupling models are not available for all four events, we only compare the influence of the coupling constraint for the 2011 Tohoku-Oki event. We compare modeled slip distributions to previously published finite fault slip inversions for each of the four ruptures. The assessment of slip distributions is done using a metric to determine the dissimilarity between the slip patterns. We first focus on the 2011 Tohoku-Oki event and compare three different rupture classes to the slip model from Minson et al. (2014) (hereafter called the "Minson model"). Two of these rupture classes utilize the coupling constrained stochastic approach, each constrained by different end member coupling models from Loveless and Meade (2016). The other class of ruptures uses a homogeneous slip potential for the stochastic approach, which can be considered the more traditional approach (e.g., Frankel et al., 2018). We obtain unique dissimilarity values for each class. For a subset of these ruptures, we model tsunami inundation for the eastern coast of Japan between 35° and 41°N and compare the inundation results to a survey proceeding the 2011 tsunami by Mori et al. (2012).

After studying the Tohoku earthquake, we widen our focus to three other subduction zones and determine whether stochastic modeling has similar capabilities irrespective of rupture or region. In short, our findings will be that stochastic slip rupture modeling can reproduce "realistic" slip distributions for all **M**9+ ruptures. For the 2011 Tohoku-Oki earthquake, including the coupling constraint, has varying effects on the results: one coupling model noticeably improved the similarity to the Tohoku earthquake, and one was not able to produce any ruptures that were similar to the earthquake, indicating that in the absence of a well-constrained coupling model, assuming no coupling constraint is likely a safer choice.

We note that we use the term "realistic" in a rather confined sense. We are focused only on determining if the stochastic slip approach can create slip patterns that resemble real **M**9+ events. We do not test the "full stack" of a PTHA calculation, such as whether we can reliably reproduce yet to occur ruptures, their statistics, or rates of occurrence at a given subduction zone. These results are a basic, but fundamental, steppingstone for assessing the applicability of the stochastic slip methodology for use at other subduction zones and future great earthquakes.

In this sense, the findings of this work still leave uncertainty in the full distribution of potential synthetic ruptures produced by stochastic modeling. For strong certainty and confidence in stochastic slip rupture modeling when applied to hazards related studies, we not only need to know if the process has the potential to reproduce slip patterns seen in previous large earthquakes, but also if the general patterns produced in all other synthetic ruptures are representative of the global history of earthquakes. This latter question is very challenging and the subject of ongoing work. As a community, we do not yet understand global earthquake history and slip potentials as well as needed to answer that question. Instead, here we inch closer to that full answer by assessing the ability of the stochastic slip approach for producing slip distributions similar to the subset of **M**9+ ruptures we have observed in instrumental times.

2. Data and Methods

2.1. Input Models

2.1.1. Slip Models

In this study, we will focus first on the 2011 **M**9 Tohoku-Oki event first since it is the best studied great earthquake (Lay, 2018); however, we will also make note of three other **M**9+ ruptures in Section 3.3. The ruptures calculated using the coupling constraint technique, along with ones generated without the constraint, will be compared to a slip distribution model for the 2011 **M**9 Tohoku-Oki rupture.

The Honshu Island region of Japan is the most densely instrumented area globally for geophysics-based observations. The dense instrumentation and the great societal impact of the rupture made this event of wide interest to the scientific community (see Lay, 2018 for a review)—well over 50 slip inversions have been calculated. Nine example slip inversions are shown in Figure 1. Rupture dimensions of slip models range from 475 to 600 km along strike and 200–275 km along dip. While there is some variability between these models, they all image a large slip asperity centered at 38°N. Some of the inversions were determined from teleseismic body and/or long

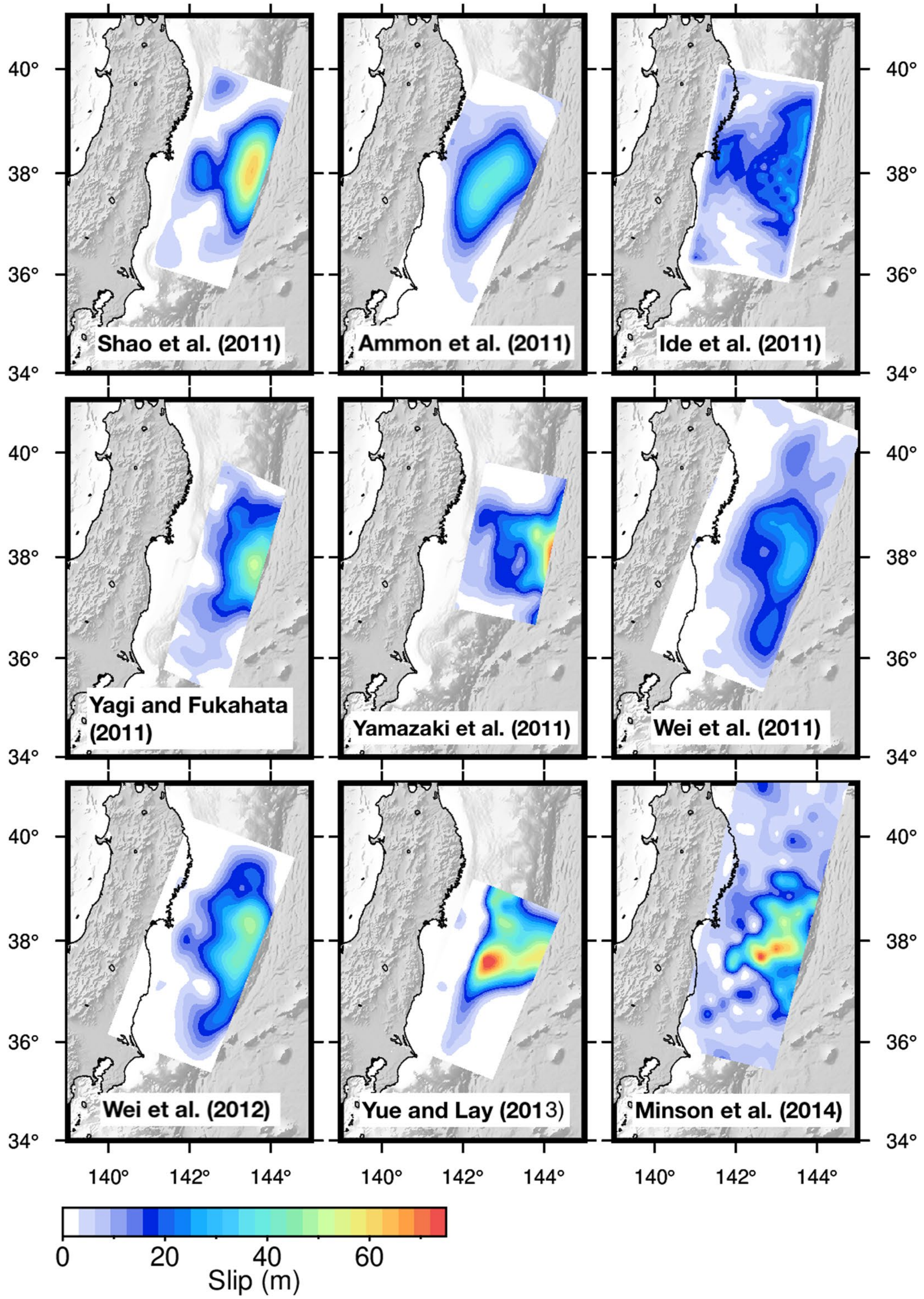

Figure 1. Nine example finite fault slip inversions for the 2011 Tohoku-Oki earthquake.

period surface waves (Ide et al., 2011; Shao et al., 2011; Yagi & Fukahata, 2011), GPS and strong ground motions (Wei et al., 2012), tsunami data, or any combination of multiple techniques and datasets (Ammon et al., 2011; Minson et al., 2014; Wei et al., 2011; Yamazaki et al., 2011; Yue & Lay, 2013). Out of these nine models, only Yue and Lay (2013) and Minson et al. (2014) combined all listed data types. Of all previously determined models for the 2011 Tohoku-Oki earthquake, the Minson model is particularly compelling because it is a Bayesian non-linear inversion. Peak slip ranges from 45 to 75 m between models, and while there is still considerable uncertainty involving the "exact" nature of the coseismic slip distribution, most of these inversions share similar features like their dominant slip asperity shape and location, and their shallow high slip. For instance, the Minson model has a very similar slip pattern to Yue and Lay (2013), Wei et al. (2012), and Yagi and Fukahata (2011).

For our comparison between stochastic ruptures and aimed slip we focus on only one of the models for the earthquake from Minson et al. (2014) expressed in Figure 2a. This model concentrates most of the slip of the rupture between 10 and 20 km in depth, with the magnitude of slip reaching 75 m high within this region. As stated prior, the Minson model is a fully Bayesian inversion, determined from simultaneously inverting for 1 Hz kinematic high-rate GNSS data, static GNSS offsets, seafloor geodesy, and tsunami data. For these reasons, and because it still shares many similarities with other inversions, we consider it to be one of the best resolved slip distributions for the earthquake.

For the other global earthquakes, we similarly focus on one slip model for each event. We utilize the finite fault slip inversion from Ho et al. (2019) ("Ho model," Figure 2c) for the 1960 **M**9.2–9.4 Chile event. The inversion was determined by jointly inverting tsunami waveforms and local geodetic data obtained from post-event leveling surveys. The model indicates slip extending along-strike for over 800 and 150 km along-dip. Slip is concentrated in three large slip asperities, each with a width of about 200–300 km and magnitude of peak slip around 40 m.

For the 2004 **M**9.1–9.3 Sumatra, we implement the inversion from Rhie et al. (2007) ("Rhie model"). This model was calculated by jointly inverting long period teleseismic data and local geodetic surface displacements (Figure 2d). One large slip asperity (~40 m) occurs in the southern portion of the rupture zone; however, slip extends almost 1,300 km along the Nicobar-Andaman Island chain. The relative size of the asperity is quite small in relation to the rupture region where more dispersed small slip occurs. Several other slip models have been proposed for this rupture (e.g., Ammon et al., 2005; Bletery et al., 2016; Gopinathan et al., 2017; Ji, 2005), however, these models utilize either teleseismic data or geodetic and tsunami data only for their inversions. So, we focus here on only the Rhie model for comparison against the stochastic ruptures calculated.

Lastly, we use the inversion model determined by Ichinose et al. (2007) for the 1964 **M**9.2 Alaska earthquake. Suito and Freymueller (2009) also presented a model for this rupture, however, we focus on the Ichinose model as it is expressed with finer resolution. Both inversions depict very similar slip patterns so either model would suffice as the example. The Ichinose model was calculated using a least squares inversion of teleseismic P waves, tide gauge data, and geodetic leveling surveys. Here, a 680 km segment of the Aleutian megathrust is modeled with a peak slip of 14.9 m and a mean slip of 4.9 m across the domain (Figure 9b). There are three dominant asperities along the Aleutian megathrust with peak slip values noticeably smaller than the three previous ruptures. In combination with the megathrust rupture, slip propagated along the Patton Bay splay fault (PBF) with a higher peak slip of 17.4 m (Ichinose et al., 2007). 10 m of uplift that was observed that was predominantly resulted from the PBF slip (Plafker, 1967). For this study we do not include the PBF in our synthetic slip models.

2.1.2. Interseismic Coupling Models

Where interseismic coupling models are available, we want to utilize these as the background slip models in the coupling constrained stochastic approach presented in Section 2.2. However, since reliable GNSS data prior to the rupture is only available at the Japan Trench, we only include coupling models for this region in our Tohoku example. The other three global ruptures presented in this study do not include the coupling constraint.

We look at two different slip deficit rate (SDR) models for the Japan Trench from Loveless and Meade (2016) (Figure 3). These models will be used as "background" models implemented in the stochastic method to constrain output slip patterns. Both models are constrained using roughly 19 years (1996–2014) of geodetic observations from the national geodetic network for Japan (GEONET). The time-series data is split into five, 3.75-year epochs and the SDR models are determined using the block model approach from Meade and Loveless (2009). The final SDR models are calculated by taking the average of the results of the five epochs. The models are determined using the same inputs as one another; however, they vary based on an imposed constraint of coupling (or no coupling) at the trench. Figure 3a imposes a constraint that the shallowest portion of the subduction zone creeps at an equal rate as the Pacific Plate rate. This model follows the idea that the shallowest portion of the megathrust cannot accumulate interseismic elastic strain. This is posited to be the result of the high percentage of clay composition at the trench (Oleskevich et al., 1999). On the other hand, the model in Figure 3b eases this

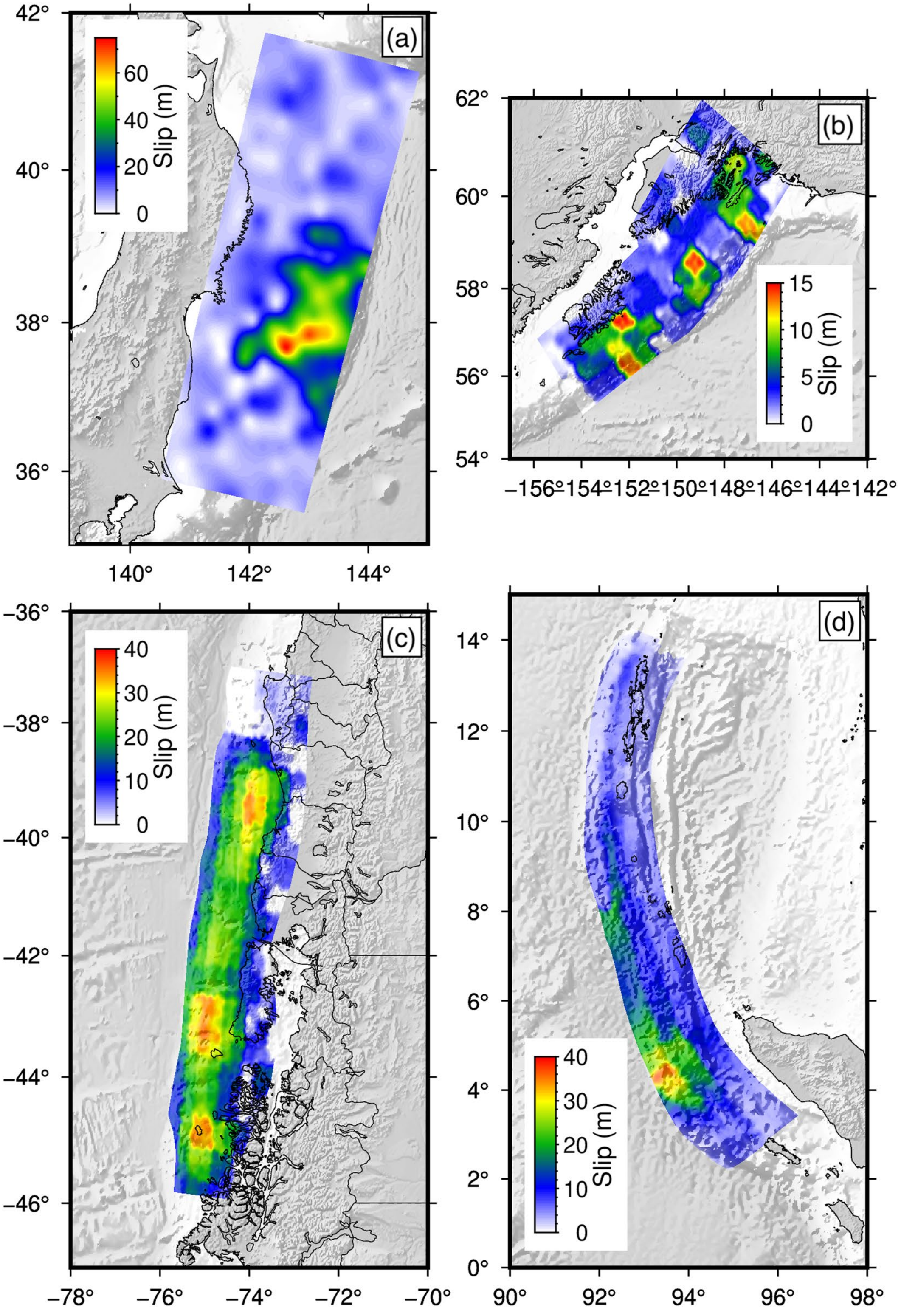

Figure 2. Slip models used in this study. (a) 2011 **M**9.1 Tohoku rupture model from Minson et al. (2014). (b) 1964 **M**9.2 Alaska rupture model from Ichinose et al. (2007). (c) 1960 **M**9.2–9.4 Chile rupture model from Ho et al. (2019). (d) 2004 **M**9.1–9.3 Sumatra rupture model from Rhie et al. (2007).

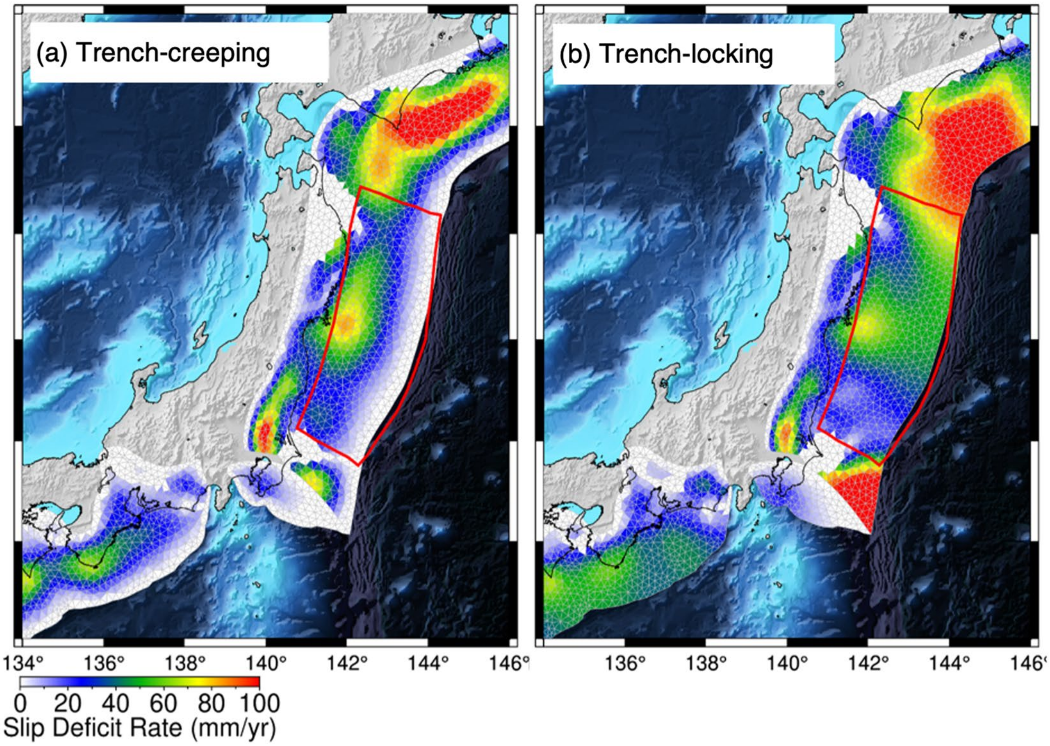

Figure 3. Slip deficit rate (SDR) models for the Japan Trench region. (a) "Trench-creeping" SDR model with the imposed constraint of creeping (or SDR = 0 mm/yr) from 5 km downdip to the trench. (b) "Trench-locking" slip deficit rate (SDR) model where no constraint on coupling near the trench so slip deficit is present up to the trench. Both coupling models come from Loveless and Meade (2016). Red outline follows the Minson model that is used as the domain for the synthetic models.

constraint, permitting variable coupling to occur up to the trench. Due to the lack of instrumentation offshore, the shallowest portions of the megathrust are poorly resolved, evident by the wide variability in SDR between the two models predominantly in the shallowest depths. Without more robust offshore GNSS instrumentation, determining which model is more accurate is nearly impossible. Therefore, we utilize both models for the study.

2.2. Stochastic Modeling

Here, we briefly detail the method of stochastic modeling, as well as how coupling patterns are introduced in the process to inform the resultant slip models. These methods can be found described in greater detail in LeVeque et al. (2016), Melgar et al. (2016), and Small and Melgar (2021). The process described below is for the Tohoku rupture case. The same process is used for the other global ruptures without the addition of the coupling constraint.

The first step is to define the megathrust as a 3D mesh surface composed of discrete subfaults using the three-dimensional finite element mesh generator, GMSH (Geuzaine & Remacle, 2009). The slab mesh is generated with the Slab2 model from Hayes et al. (2018) with an average subfault vertex length of 15 km. We constrain the 3D mesh to the domain of slip in the Minson model rather than using the entirety of the Japan subduction zone. Recall, our focus here is only to test the ability of the stochastic approach to reproduce rupture patterns. Since we are only focused on creating ruptures with "realistic" slip patterns, we do not worry about utilizing a full subduction zone domain to model on. This same process is used for the Sumatra case, where the rupture domain is defined from Slab2. For the Chile case, we utilize the slab model from Rodriguez and Russo (2020) rather than the Slab2 since the latter does not reach the entirety of our rupture domain. For the Alaska case, however, we maintain a simple rectangular domain that follows the Ichinose model. Rather than modeling in 3D, we maintain a simple geometry because interpolating from the original fault geometry from Gudmundsson and Sambridge (1998) to Slab2.0 would create too many irregularities and potentially alter the magnitude of the interpolated model.

Once the mesh is defined, a subfault is selected at random as the synthetic rupture hypocenter. For a given target magnitude, the rupture length and width are determined based on a probabilistic scaling law (Blaser et al., 2010), which for any earthquake magnitude lead to a log-normal distribution of length and width. As the rupture magnitude increases, the dimensions of the rupture also on average increase. The log-normal distribution allows for variability within the dimensions of ruptures of equal magnitude.

Then, we utilize the method of stochastic modeling introduced by Mai and Beroza (2002) to calculate the rupture itself. Mai and Beroza (2002) determined that the autocorrelation function that best represents slip as a spatially random field is the von Karman autocorrelation function (VK ACF),

$$P(k) = \frac{a_x a_z}{(1+k^2)^{H+1}}, \tag{1}$$

where the a denotes the correlation lengths along-strike and downdip, H is the Hurst exponent, and k is the wavenumber. The correlation lengths principally describe the dominant asperity size of the ruptures. As the magnitude and dimensions of a rupture increases, the correlation lengths also increase. With the VK ACF, there are only three necessary assumptions needed to define earthquake slip patterns: the correlation lengths in the along-strike and down-dip, and the Hurst exponent that models the roughness of the slip pattern. We apply the results from Melgar and Hayes (2019) for defining correlation lengths based on a log-linear scaling of magnitude and correlation lengths and a magnitude independent Hurst exponent.

The method above is expressed in the spectral domain of slip rather than the spatial domain. To account for 3D fault geometries and enforce prior constraints (e.g., geodetic coupling), we apply the Karhunen-Loeve (K-L) expansion to the VK-ACF, where slip can now be represented spatially (LeVeque et al., 2016). The K-L expansion states that a slip vector, s, is described as

$$s^g = \mu^g + \Sigma_{k=1}^{N} z_k \sqrt{\lambda_k^g v_k^g}. \tag{2}$$

This defines s as the sum of the background slip model, μ, and the summation over the desired number of eigenmodes, N, of the eigenvalues and eigenvectors from the VK-ACF, λ_k and v_k. Further stochastic behavior of the resultant ruptures is included in the equation thanks to z_k, which defines a normally distributed set of random numbers with a mean of 0 and a standard deviation of 1. The variable z allows us to create any number of unique slip distributions for a given magnitude and rupture dimensions. A difficulty that arises in using the K-L expansion is the possibility of producing negative slip values. Negative slip would produce normal faulting behavior, inconsistent to the desired sense of faulting. This is not observed in nature, so, to remedy it LeVeque et al. (2016) used a lognormal distribution that inherently restricts slip values to be strictly positive. In Equation 2, the superscript g denotes a lognormal distribution.

For ruptures where all subfaults have equal potential for slip and no prior constraints are applied, μ is simply a homogeneous mean model with enough slip to match the desired target magnitude. However, we can instead impose a mean slip model that is informed by the coupling pattern as μ. For instance, for a given desired magnitude and rupture dimensions are selected from the scaling laws, the coupling pattern in the segment is re-scaled into slip pattern. This is then used as μ and stochastic variability is applied to create the output ruptures.

In this method, the coupling model does not inform how much slip will occur at a given location. But rather, it provides a greater probability for areas of high SDR to have greater coseismic slip. It is still possible in this method for a region of high SDR to rupture in smaller slip than a region with relatively smaller SDR. In this method however, regions where SDR = 0 should not produce coseismic slip. The actual influence of the coupling constraint is often difficult to discern for a single given rupture, but in observation with a large suite of ruptures, the mean pattern of slip for all the ruptures in the suite resembles the initial coupling pattern constraint.

To calculate the ruptures, we use the Fakequakes implementation of the aforementioned methods. This is a module of the open-source forward modeling and inversion code MudPy (Melgar & Bock, 2015; Melgar, LeVeque et al., 2016; Small & Melgar, 2021). Fakequakes can calculate both homogeneous and coupling constrained synthetic rupture models. For each of the three classes mentioned prior, we calculated a total of 4,000 ruptures with starting magnitudes between **M**8.8 and **M**9.1 in magnitude bins of 0.1. The maximum slip on any given subfault is limited to 100 m. Although this is quite large, the 2011 Tohoku-Oki event is considered to have slipped over 70 m in some patches (Minson et al., 2014). The rupture domain lies between 35°N and 41°N, with a down dip limit of slip at 50 km depth. The domain follows the slip region of the Minson model (Figure 2a). Rupture area and magnitude are unconstrained, so any portion of the domain may be considered or neglected, and the final magnitude for a given area may vary from the starting magnitude based on dimensions and scaling laws. We also leave the hypocenter location unconstrained, the code selects at random any subfault to nucleate the rupture. For the coupling constrained stochastic models, regions where the SDR is 0 cannot slip nor act as the hypocenter. A Hurst exponent of 0.75 is used along with all eigenmodes (equal to the number of subfaults) in our models. Typically for tsunami modeling purposes, a smaller amount of eigenmodes can be used to reasonably represent a rupture (LeVeque et al., 2016); however, here we use all eigenmodes in order to reduce possibilities of uncertainty.

Similar Fakequakes setup for homogeneous mean model ruptures is implemented for the other **M**9+ earthquakes. For each of the global ruptures, we model 2,500 ruptures in 0.1 magnitude bins. Since we do not include the coupling constraint for the global ruptures, ruptures are only calculated with the homogeneous background model. Like the Tohoku case, rupture area and magnitude are unconstrained and a downdip limit of 50 km depth is applied. More information on the setup for the other events is described in Section 3.3.

2.3. The Dissimilarity Metric

Since we are interested in comparing the generated stochastic slip distributions to known slip inversions, it is important to define a quantitative assessment of likeness between models. To do this, we calculate the numerical dissimilarity between ruptures using the normalized square metric (Kragh & Christie, 2002; Razafindrakoto et al., 2015). There are other metrics for quantifying dissimilarity (e.g., gray scale metric, Wilson et al., 1997), however, we focus on the normalized square metric as it is both numerically simple and efficient.

In comparison to other dissimilarity metrics, the normalized square metric is best for capturing the magnitude differences between two objects and is sensitive to image translation. The normalized square mean metric expresses dissimilarity, D, as

$$D(A,B) = 100\frac{\Sigma_i[A(i)-B(i)]^2}{\left(\Sigma_i[A(i)]^2+\Sigma_i[B(i)]^2\right)/2}. \tag{3}$$

Dissimilarity between two slip models, A and B, is expressed as the sum of square of the difference between the models individual subfaults divided by the mean of the individual squared values. A and B in the equation are regular grids of subfaults. Prior to interpolating to a regular grid, we first interpolated the Minson model to the Slab2 geometry to maintain uniformity in the process. We then interpolate the 3D triangular mesh ruptures and slip model using the spline interpolation method.

Kragh and Christie (2002) previously define this metric as a percentage with values between 0% and 200%. The more dissimilar the two models are from one another, the greater the value. $D = 0$ denotes identical slip models and the greater the differences between the two models, the greater the value of D is. For ease of understanding, we scale the dissimilarity metric by dividing it by two, making it a metric from 0 to 100.

2.4. Tsunami Inundation Modeling

Although the dissimilarity value provides a basis for quantifying likeness between the slip models, only analyzing the one metric may still produce uncertainty in determining whether a rupture is realistic when compared to the earthquake model of focus. While low dissimilarity between a stochastic model and the inversion is encouraging, there is no clear distinction on what values of dissimilarity qualify as “good enough” for considering one of the hypothetical ruptures comparable to the specific slip inversion. To determine the dissimilarity values that can be considered, for example, “Tohoku-like,” we take the extra step of modeling tsunami inundation and compare inundation values to recorded survey points. Specifically, we compare how well our synthetic ruptures can match the post-event survey points from Mori et al. (2012) based on the percentage of points inundated and their inundation heights. This analysis provides an observable phenomenological rationale for comparing impacts of ruptures since the rupture pattern directly controls the extent of the tsunami. We note here that only inundation modeling in this study is done so for the Tohoku example. The other three rupture cases do not have as extensive inundation surveying following the tsunamis as did the Tohoku event. Though we cannot directly compare the phenomenological observations for the other global ruptures, we cautiously utilize the results from the Tohoku case in the global rupture analyses.

Post-event tsunami inundation surveys measure the maximum height of the tsunami wave propagation onshore. Here, we define inundation with respect to mean sea level. We model inundation at 3,244 survey points from Mori

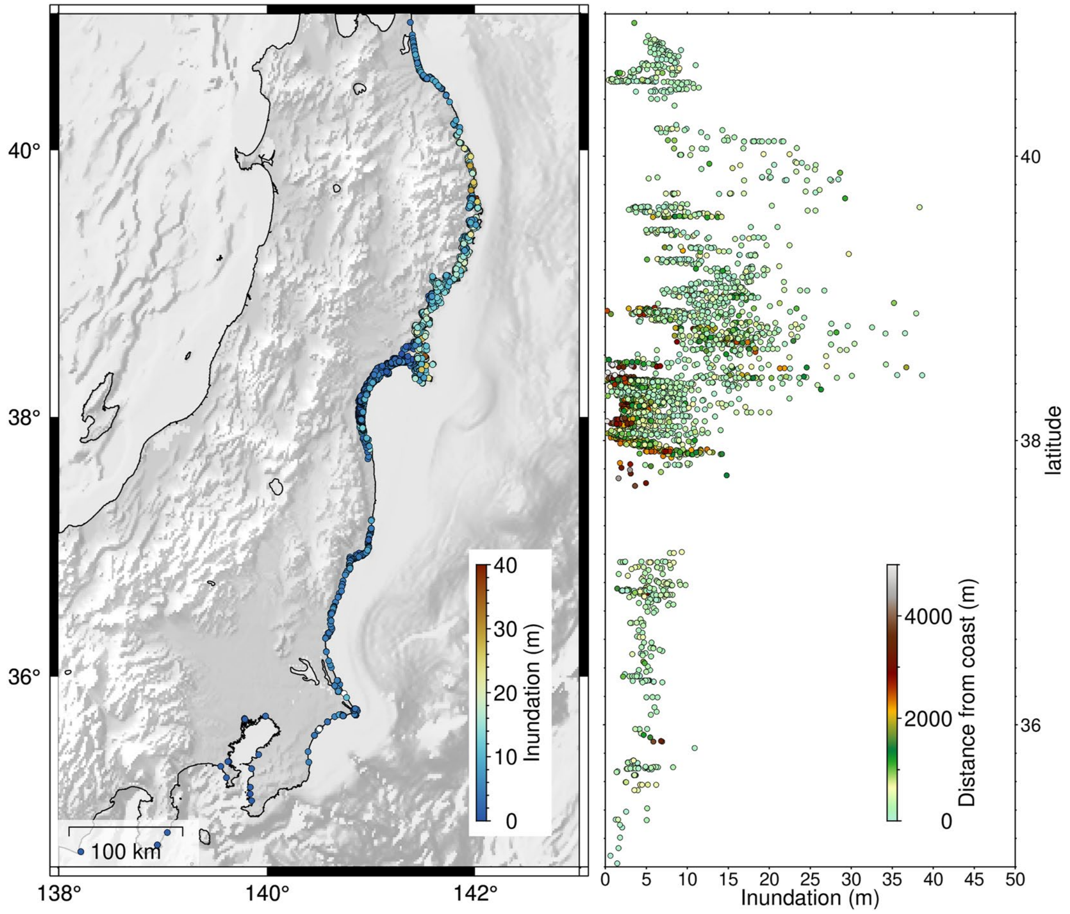

Figure 4. Tsunami inundation survey of the 2011 Tohoku-Oki tsunami from Mori et al. (2012). (a) Map view depiction of survey points where color scale depicts recorded inundation height in meters. (b) Plot of tsunami inundation versus latitude with the color scale depicting the distance the survey point is from the coast. Most recorded points are less than 100 m from the coast, but in the Sendai Plain (~38°N) points are recorded several kilometers from the coast.

et al. (2012) (Figure 4). In the study, they record over 5,000 total tsunami data points onshore between 35° and 41°N. In their data set, they also record run-up height, which is the maximum height the tsunami propagated to onshore (the run-up distance) with respect to sea level. We do not consider these points for our study since modeling for run-up distance and height is difficult. The data set for inundation is extensive along the coast, however, a gap in data between roughly 37–38°N is present. Data distribution is not recorded equally along the coast, with the greatest abundance of points in the Sendai Bay and Sanriku Coast in Iwate Prefecture (37.5–38.4°N). The inundation points range from 0 to 40 m in height, with over 75% of all inundation points below 10 m. Some inundation points are also recorded as far as 5 km inland, but the majority of the points occur less than 1 km from the shore.

To model tsunami inundation for calculated ruptures, we first must determine the resultant coseismic vertical deformation to be applied as the initial condition for tsunami wave generation. We utilize the analytical solution for angular dislocation for triangular subfaults in an elastic half space (Comninou & Dundurs, 1975), which is an adaptation of the Okada equations for rectangular subfaults (Okada, 1985). We use the radially symmetric Earth structure model from Gregor et al. (2002) developed for the Cascadia subduction zone for calculating the surface deformations. Tsunami inundation is calculated using the finite volume, 2D depth-average, non-linear tsunami modeling code Geoclaw (http://www.clawpack.org/geoclaw) (LeVeque et al., 2011). We assume an instantaneous starting condition since rupture propagation velocities are much faster than tsunami wave velocities (e.g., Williamson et al., 2019).

We model tsunami generation and inundation for points between 34.5° and 41°N. Topography and shallow water bathymetry must be sampled with very fine resolution for accurate inundation modeling. Because our modeled domain is quite extensive (7° in latitude and longitude) and we need fine resolution bathymetry and topography data for coastal regions, we utilize one coarser bathymetry/topography file for the entire domain and finer scale subregions for the coastal areas of interest to decrease computational cost. We use SRTM15 with a sampling rate of 15 arcseconds (∼450 m pixels) for our overall bathymetry/topography domain (Tozer et al., 2019). We then stitch together SRTM1 topographic data (1 arcsecond sampling rate, ∼30 m pixels) and 1 arcsecond bathymetry data from the "M7000" data set purchased from the Japan Hydrographic Association in eight rectangular segments that extend to 200 m below sea level between 34.5°N and 41°N. We resample these fine segments from 1 to 3 arcseconds as 1 arcsecond was too costly for the tsunami models to run even with 40 CPUs in hand. To increase efficiency even more, we utilize the adaptive mesh refinement (AMR) within GeoClaw where the more complex portions of tsunami propagation occur and proximity to regions of interest decrease, the mesh can adaptively become finer. We use five different AMR levels that go from coarsest to finest: 2', 1', 30", 15", and 3", respectively.

Even with these capabilities, modeling inundation for over 3,000 points along a region of 7° latitude is costly. Using 25 threads, each tsunami inundation model took over 4 hr to complete. So, rather than calculating all 12,000 tsunami models, we instead took a subset of ruptures, totaling 330. These ruptures were chosen at random, however, we favored adding more ruptures with lower dissimilarities (below $D = 50$). Since our main interest is determining the efficacy of the von Karman ACF stochastic approach at producing great earthquakes, our focus is naturally on the lowest valued dissimilarities. From Equation 3, the more similar the stochastic model is to the slip inversion, the lower the dissimilarity value is. So, lower dissimilarity ruptures become increasingly more important than larger valued ones. For each of the runs, we compare the inundation residual between the modeled points and the surveyed points using the root mean squared error (RMSE), and we also look at the percentage of points inundated, regardless of inundation height. We utilize the RMSE rather than another statistical metric as it allows us to directly observe error in the same dimensions as our data. The inundation percentage on the other hand, allows us to observe a simpler binary statistical measure.

3. Results

3.1. Rupture Modeling and Dissimilarity for the Tohoku-Oki Case

In total, 12,000 ruptures were generated and split evenly between the three different rupture classes. Although initial magnitudes range from **M**8.8 to 9.1, final magnitudes fall between **M**8.6 and 9.4 since we modeled ruptures without magnitude constraint. All three ruptures classes have similar distributions of final magnitudes. Rupture dimensions vary across the fault zone, however, due to the more confined model domain where ruptures may propagate over, there is a tendency for ruptures to slip the entire domain.

For all ruptures, we calculate the dissimilarity between the slip distribution and the Minson model using the normalized squared metric. The values for all ruptures are shown in Figures 5a–5c, where they are plotted in histograms based on rupture class. From the histograms, we can split the three classes into two distinct groups based on their distributions of dissimilarity values. The trench-creeping class produces ruptures with higher values than the other two classes, with a minimum value of 35. The distribution has a mode around a dissimilarity of 60. The trench-locking and homogeneous classes, on the other hand, have a dissimilarity distribution relatively like one another. The minimum dissimilarity for the two classes is 12 for the trench-locking and 16 for the homogeneous class. To first order, the two classes appear to have similar rupture dissimilarity distributions, yet there is a tendency in the trench-locking ruptures toward lower values overall. In comparison to the trench-creeping class, the homogeneous class has almost 400 ruptures below the least dissimilar trench-creeping rupture, about 10% of the total homogeneous ruptures. The trench-locking class, however, has almost 600 ruptures below the trench-creeping class, or 15%.

From these dissimilarity values, we would like to better understand at what dissimilarity value can a rupture most likely be considered "Tohoku-like." The accompanying rupture models in Figure 5 show three ruptures for each class with varying rupture dissimilarities. We generally see noticeable differences between ruptures with the lowest dissimilarities (Figures 5g–5j) and the highest dissimilarity (Figures 5f–5l). Besides the lowest dissimilarity ruptures, it is difficult to confidently distinguish just by observation which rupture has the lower dissimilarity in the second two columns.

There is a trend for ruptures below a value of 35 to have large slip patches around 38°N and between 10 and 30 km downdip similar to the Minson model. Because the normalized square metric assesses dissimilarity by a point-by-point comparison, even if a rupture has a similar asperity size and shape to the Minson model, if the location of the patch is offset, this will influence the dissimilarity outcome. This metric is also more heavily affected by larger slip differences. So, if larger slip patches are not represented or expressed in other areas than

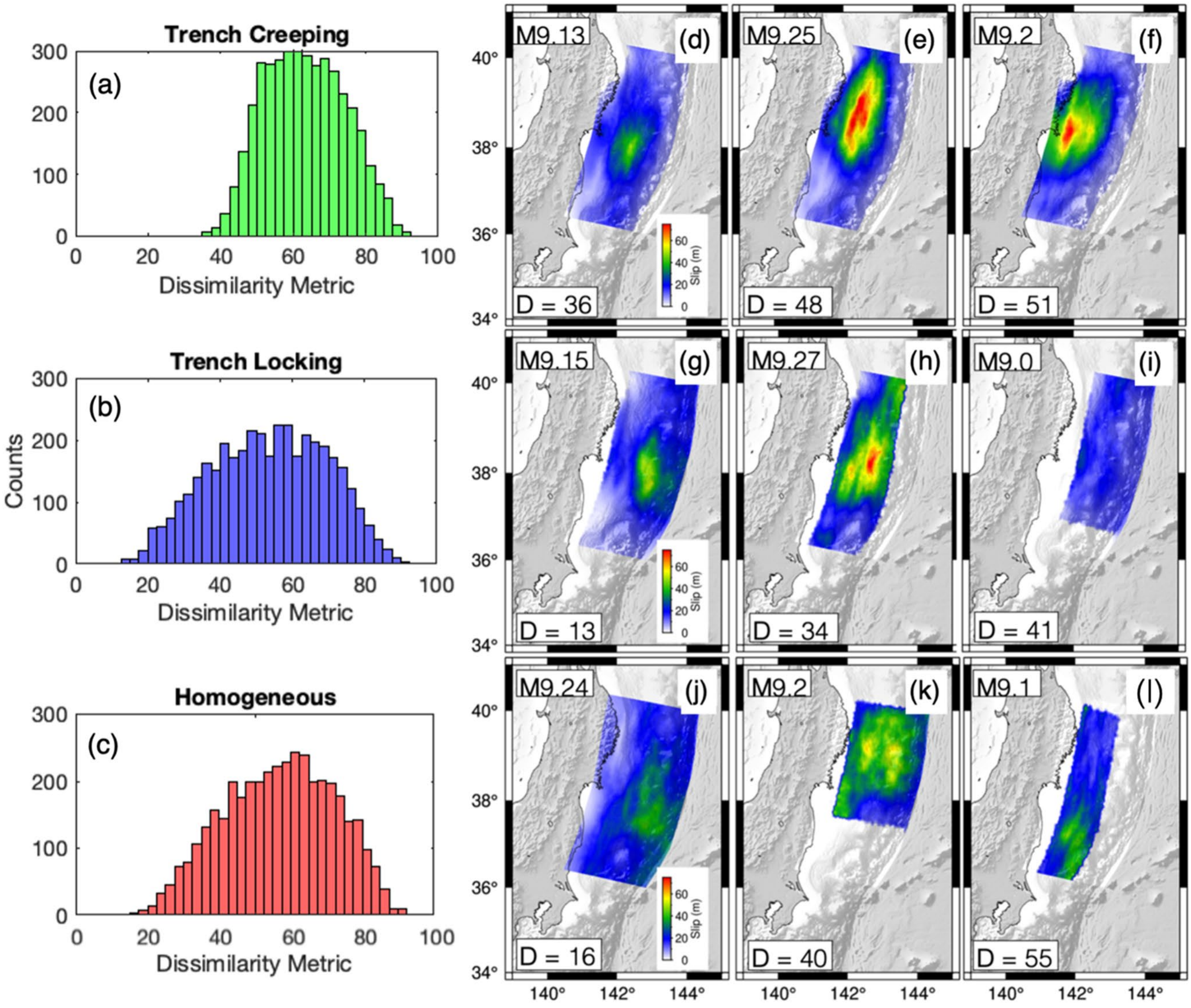

Figure 5. (a–c) Dissimilarity metric histograms with a bin width of 2.5 for the three rupture classes. (d–f) Example stochastic rupture slip models with varying dissimilarity values, D, for the trench-locking class, with lowest values toward the left. Rupture magnitudes are presented in the top left corner of each map. (g–i) Same as above but for the trench-locking class. (j–l) Same as above but for the homogeneous class.

the location of the Minson large slip patch, this negatively influences the outcome dissimilarity. As the rupture dissimilarities increase, the variability in the patterns of slip distribution increases. For instance, some ruptures with larger dissimilarities do not rupture up-dip and some experience their largest slip patches farther North or South of the Tohoku slip patch in disagreement to the Tohoku earthquake.

3.2. Tsunami Inundation Results for the Tohoku-Oki Case

Dissimilarity alone is a useful metric to determine a rupture's likeness to the slip model; however, there is some ambiguity by using the metric alone. Thus, we include inundation modeling as an extra dimension of likeness. By observing both inundation and dissimilarity, we can have a better sense of the finer differences between ruptures of variable dissimilarities.

Along with modeling tsunami propagation for the 330 synthetic ruptures, we model tsunami inundation as a result of the Minson inversion to establish a comparison baseline. All applied conditions for tsunami propagation are the same for the Minson scenario in comparison to the stochastic models. The Minson slip model can inundate 91% of all inundation points and fits with an RMSE of 7.1 m. The synthetic ruptures, on the other hand, have a spread of RMSE

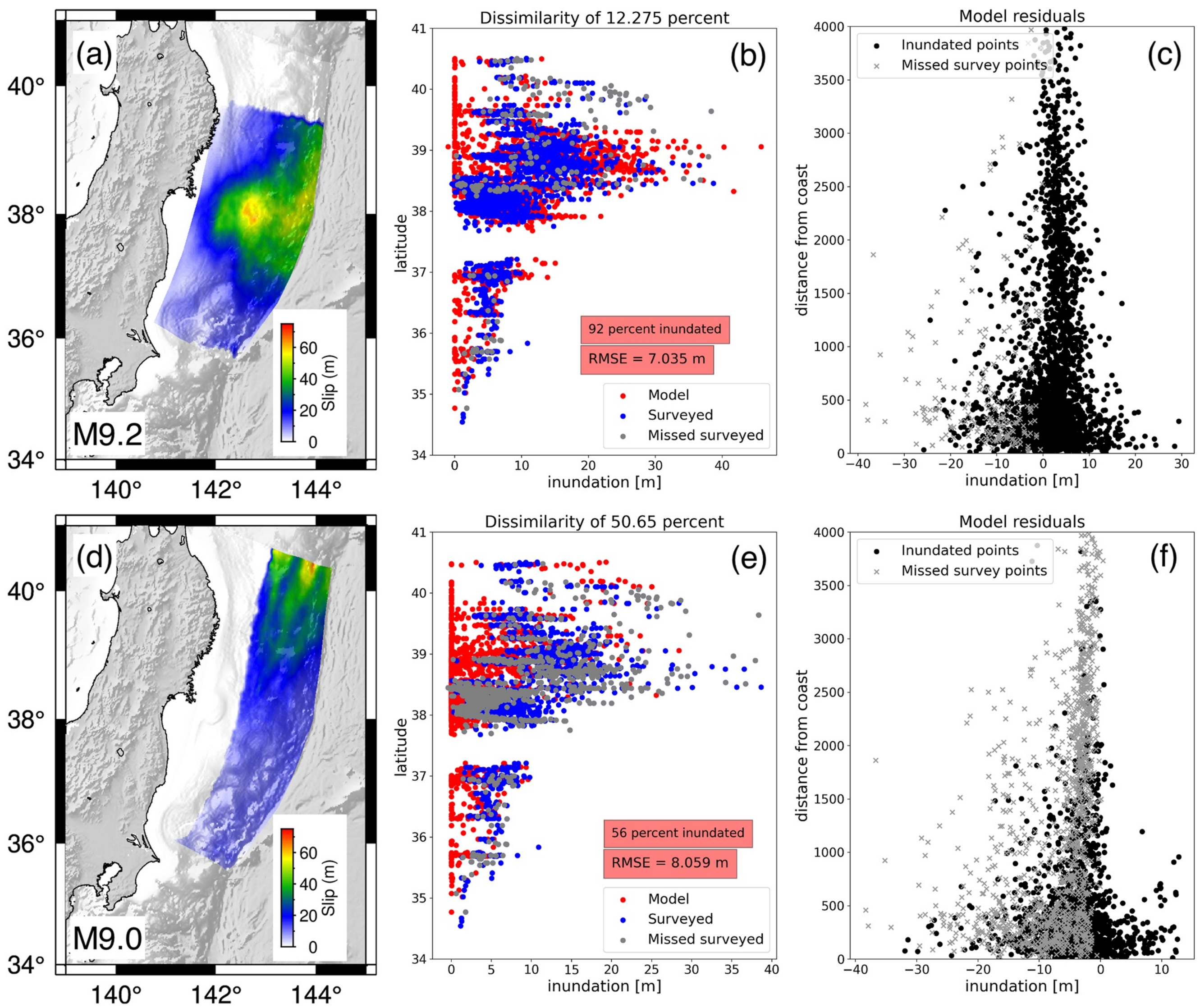

Figure 6. (a) **M**9.2 rupture model in the trench-locking class. (b) Inundation in meters at each of the survey point locations versus latitude. Points are color coded as red, blue, and gray for the modeled points from the rupture in (a), the recorded survey points, and the missed survey points that did not get inundated by the model, respectively. The dissimilarity value for the rupture is presented at the top of the plot. (c) Tsunami inundation residual in meters between the modeled points and the surveyed points versus the distance from the coast in meters at each point. Points are denoted by a gray X for missed surveyed points and so the residual is simply the inundation height from the survey. (d) **M**9.0 rupture model in the trench-locking class. © Same as (b) but for the rupture model in (d). (f) Same as (c) but for the rupture model in (d).

values between 7 and 10.5 m, and a large range of inundation percentages between 10% and 100%. The inundation from the Minson scenario is very well modeled, however, still with error. The Minson model has the most difficulty in accurately inundating points along the Sanriku coast where survey points record the largest wave heights. Still, it is able to inundate most points with a relatively small RMSE compared to the suite of synthetic ruptures.

Figure 6 shows two example stochastic ruptures with differing dissimilarity values and their tsunami inundation. The first example is a rupture with a low dissimilarity value of 12.3. In comparison to the post-event survey, the model inundated 92% of the 3,244 survey points. The RMSE of the inundation model is 7.03 m with respect to the survey. The modeled tsunami residuals for this rupture are biased toward the positive which represents a larger tsunami than the recorded tsunami. By considering both the very low dissimilarity value and the high percentage of points inundated from this rupture, we can say this rupture is “Tohoku-like.” In contrast, the second rupture shown has a dissimilarity much greater than the first, with $D = 50.65$. From inspection of the slip distribution, we can see that it does not contain a large shallow slip patch as required by the Minson slip inversion. This rupture rather experiences the largest slip toward the North of the domain. Its tsunami model only inundates 56% of the survey points, far less than the 92% inundation from the previous rupture. This rupture does not appear to inundate far inland from the coast—almost all survey points past 1 km do not experience inundation. We can see from this example that this rupture should not be considered "Tohoku-like" based on its high dissimilarity and fits the inundation data poorly.

If we consider all the ruptures that we performed inundation modeling for, we can understand the relative importance and "threshold" of the dissimilarity metric. In Figure 7, the dissimilarity metric is plotted with respect to the inundation percentage for all three of the rupture classes. Each scatter point is scaled by the rupture's RMSE for inundation. There is a clear distinction between ruptures with high and low dissimilarity values. The points generally follow a linear path along which the dissimilarity metric decreases, the inundation percentage increases and the RMSE decreases. So, as the ruptures approach the top left corner of the plot, the ruptures become more "Tohoku-like." There is some variability associated with these metrics, especially in the more moderate (30–60) dissimilarity values. For instance, for a given moderate dissimilarity value, inundation percentage varies by almost 40%–50%. As the dissimilarity percentage decreases, however, the degree of variability in all three metrics decreases.

To maximize the rupture's similarity to the Tohoku event and specifically the Minson model, we look for dissimilarity values that both maximize the inundation percentage and minimize the RMSE. From the results, we fit an arbitrary threshold for what can be considered a "Tohoku-like" rupture at $D = 20$. At this threshold, inundation percentage for all points is over 80% and there is the smallest variation in the distribution of inundation percentages. The RMSE for all ruptures is consistently under 8m, with an average RMSE of 7.34 m, which is over 1m smaller than the total average. Recall that the Minson model inundated 91% of the points and has an RMSE of 7.1 m. The synthetic ruptures that have a dissimilarity of under 20 generally share similar inundation results to that of the Minson model (example rupture shown in Figure 6a). There are 57 trench-locking, 14 homogeneous and 0 trench-creeping ruptures that fit this threshold. If we increase the threshold by 5, we observe 169 trench-locking 68 homogeneous, and still no trench-creeping ruptures. Although an increase in the threshold of 5 still has a dominance of ruptures with over 80% inundation and RMSE average of 7.6 m, the range in inundation results begins to widen much greater here (Figure 7). There is a general consistency in ruptures below a dissimilarity of 20, however, past 20 a sharper negative trend is present in inundation as the dissimilarity increases. So, we conservatively keep the lower threshold presented. We note that any threshold we pick is arbitrary; because of the way the dissimilarity value is calculated, there is still substantial variability in slip distributions and slip magnitudes. But, beneath this threshold for the synthetic ruptures, the dominant slip asperity is reproduced, and the tsunami metrics are fit reasonably well.

In Figure 7, there are some models that inundate almost all of the survey points but also have some of the largest RMS errors and variable dissimilarity. Though these ruptures occur across each class, the trench-creeping constraint produces the largest amount of them. These ruptures all have the common characteristic of producing a large slip patch at 30 km downdip from the trench close to the shoreline of the Sanriku Coast. The dominant slip patch for these ruptures may be relatively deep, resulting in smaller surface deformation in comparison to a slip patch further up dip; however, the proximity to the coast and the magnitude of slip (over 60 m on average) generates a large tsunami relatively close to the shore. It should be recognized here that although the inundation percentages are very high for these examples (over 95%), they have relatively large dissimilarity values and RMS errors. Even though one metric appeared similar, the combination of all three metrics is important to determine the similarity to the real rupture.

3.3. Results for Other Global Ruptures

We now broaden our focus to the results of modeling other great earthquakes to determine if this stochastic approach can reproduce previously determined slip distributions at other subduction zones. For other **M**9+ events, there are not as robust inundation surveying and calculated slip inversions as there are for the 2011 Tohoku-Oki event. For the following ruptures, we only calculate dissimilarity and visually inspect ruptures to compare the stochastic ruptures to the finite fault models. Previously, we determined a specific "threshold" for acceptable dissimilarity values for ruptures for the 2011 **M**9.1 Tohoku event. We do not directly utilize the threshold for the preceding cases, but instead compare dissimilarity values and dominant slip distribution characteristics to evaluate whether ruptures are comparable to the slip inversions. Here, we will focus on three other **M**9+ events: 1960 **M**9.3–9.4 Chile, 2004 Sumatra **M**9.2, and 1964 Alaska **M**9.2. As stated prior, we do not have reliable coupling models for any of these event locations prior to the ruptures, we only model them using the homogeneous stochastic approach. Below are the results for the three earthquakes.

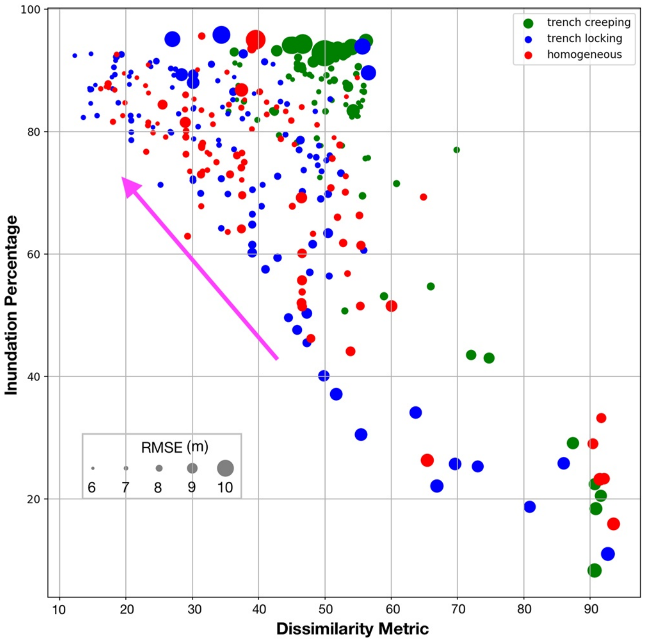

Figure 7. Dissimilarity metric versus inundation percentage plot for all 330 ruptures that we performed inundation modeling for. The points are scaled with their RMS error and color coded based on their rupture class. The arrow depicts the trend of more "Tohoku-like" ruptures based on the three metrics.

3.3.1. 1960 Chile

We model 2,500 ruptures in 0.1 magnitude bins between **M**9.2 and 9.6. The domain is constrained between 37° and 46°S along strike and a down dip limit of 50 km. The simple rectangular geometry of the Ho model is first interpolated to the same slab geometry as the stochastic ruptures prior to dissimilarity analysis. The rupture domain is subdivided into 1790 triangular subfaults, with lengths around 10 km wide on average. Final magnitudes vary from **M**8.9 to 9.7.

There is a similar distribution of dissimilarities with low values compared to the Tohoku example (Figure 8a). While we will not directly apply the threshold for the case prior, we will loosely use it as a comparison point. Figures 8c and 8d show two synthetic ruptures with varying dissimilarity values. The first matches the maximum slip observed in the Ho model well and there appears to be three distinct slip patches with similar peak slip values that correlate well with the locations seen in the Ho model. This stochastic rupture has a dissimilarity of 13, which is the lowest in the suite of ruptures and comparable to the lowest Tohoku rupture. The next rupture has a slightly higher dissimilarity of 17. Although the maximum slip observed does not reach over 30 m as opposed to the 40 m seen in the Ho model, the dominant slip patches are still relatively well resolved. As the dissimilarity value increases, the ability to resolve the three slip asperities quickly decreases. There are 75 ruptures of the 2,500 total ruptures that fit below the dissimilarity threshold determined for the Tohoku case. This is an increase in the percentage of ruptures that fall beneath the threshold in comparison to the homogeneous class for the Tohoku event (75 compared to 14 ruptures). Although we do not model tsunami inundation for the Chile case, through visual inspection and calculation of dissimilarity values, we see that this stochastic slip method is able to reproduce the Chile slip inversion reasonably well.

3.3.2. 2004 Sumatra

We now look at the 2004 **M**9.2 Sumatra event, which is the spatially longest rupture in instrumental history. Following from the previous analysis, we model 2,500 ruptures in 0.1 magnitude bins between **M**9.0 and 9.4. Since we do not fix final magnitude, final ruptures are between **M**8.8–9.6. The domain extends from 2°N to 14°N and slip is limited to above 50 km down dip, with a total of 1,084 subfaults of around 20–25 km in length

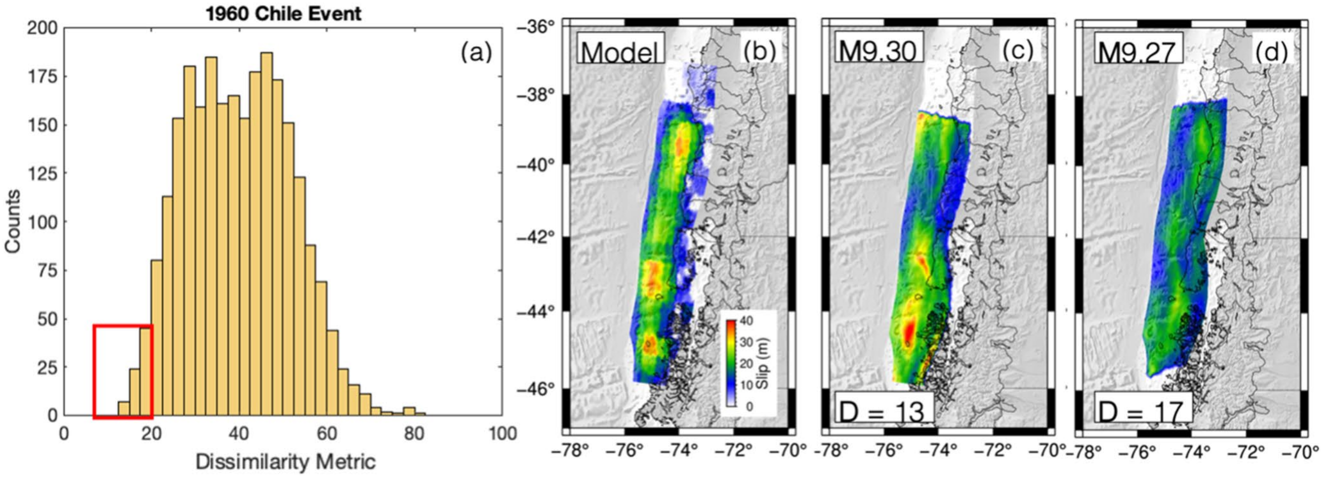

Figure 8. (a) Dissimilarity histogram distribution with a bin width of 2.5 for the 1960 Chile rupture. Red box indicates ruptures below the Tohoku case threshold. (b) Slip model from Ho et al. (2019) that is used as the model we are trying to reproduce with the stochastic ruptures. (c) Example **M**9.3 rupture that has the lowest dissimilarity compared to any other modeled rupture. Color is represented by slip in meters shown in (a). (d) Same as (c) but for a **M**9.27 rupture and a slightly larger dissimilarity, but still beneath the threshold of dissimilarity.

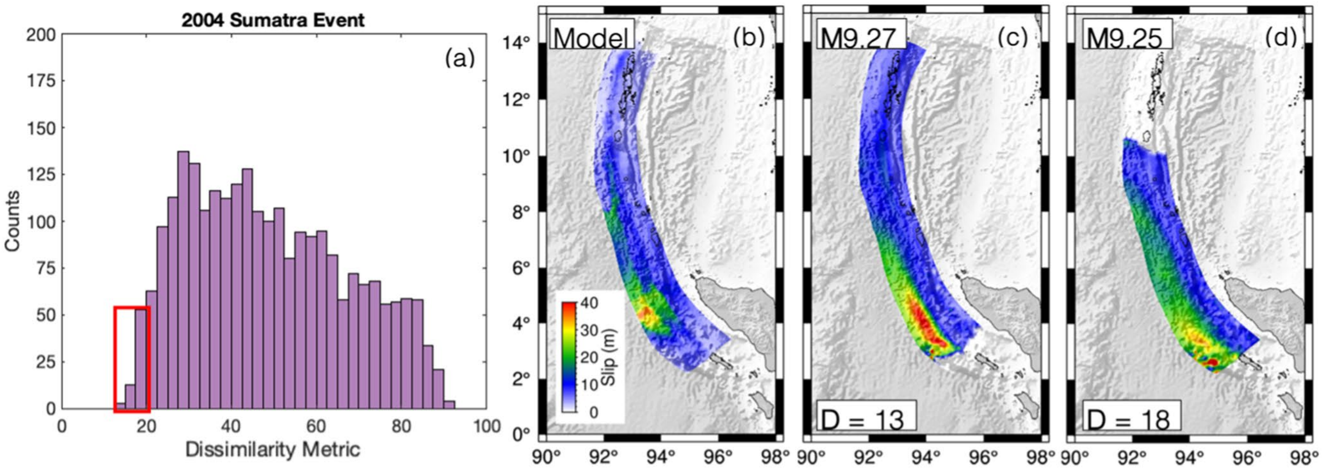

Figure 9. (a) Dissimilarity histogram distribution with a bin width of 2.5 for the 2004 Sumatra rupture. Red box indicates ruptures below the Tohoku case threshold. (b) Slip model from Rhie et al. (2007) that is used as the model we are trying to reproduce with the stochastic ruptures. (c) Example **M**9.27 rupture that has the lowest dissimilarity compared to any other modeled rupture. Color is represented by slip in meters shown in (a). (d) Same as (c) but for a **M**9.25 rupture and a larger dissimilarity.

each. The Rhie model is first interpolated to the domain geometry and then both ruptures and the slip model are interpolated to a regular grid for the dissimilarity analysis.

Figure 9 shows two examples of rupture models that have relatively low dissimilarity values. The first rupture (Figure 9c) has a large slip patch with similar peak slip as the Rhie model and dispersed smaller slip (10 m and below) throughout the rest of the model. The slip patch extends further south along the subduction zone than the Rhie model. The second rupture shown has a slightly higher dissimilarity value and is smaller than the Rhie model (Figure 9d). Its dominant slip patch is located further south but close to the Rhie model and has more scattered larger slip throughout the model.

Like the Chile example, we cannot completely apply the Tohoku dissimilarity threshold to the Sumatra case. Instead, we still consider it while also using visual inspection to determine likeness. There are 79 out of the 2,500 ruptures that have dissimilarity values below the threshold, which is greater than any of the rupture classes for Japan or Chile. Within these ruptures that fall within the Tohoku threshold, all have either a dominant slip patch centered around 3°–4°N or dispersed slip throughout the entire domain. As the dissimilarity increases, the magnitude and size of the slip patch or the extent of the background slip varies more substantially. This variation is noticed in the two examples shown below. The lowest dissimilarity ruptures ($D < 15.5$) have both the dominant slip patch and the dispersed slip along most of the domain. There are 6 ruptures that have large slip patches with similar peak slip values and background slip that extends through most of the subduction zone. All the ruptures that fall below the previous Tohoku dissimilarity threshold on average express the dominant trends characterized by the Rhie model. Even though the Sumatra rupture is spatially larger and has relatively more dispersed slip throughout, stochastic modeling is still able to reproduce the slip inversion well.

3.3.3. 1964 Alaska

Our final earthquake of interest is the 1964 **M**9.2 Alaska event, the largest earthquake to occur in North America and the second largest globally in instrumental history. Once more, we model 2,500 ruptures in a 0.1 magnitude bin size between **M**9.0–9.4. We do not interpolate the Ichinose model and calculate ruptures along the Ichinose model domain with 765 rectangular subfaults of size 16 × 16 km.

In Figure 10, we show the dissimilarity values for all 2,500 ruptures along with two ruptures with low dissimilarity to compare against the slip model. Compared to the other **M**9+ earthquakes, the Alaska event is not able to be fit with as low of dissimilarity values. Similar to the Tohoku case, the distribution of rupture dissimilarities is quite similar still. The mode of dissimilarity values for the homogeneous class of the Tohoku ruptures is around 50, matching the Alaska case well. There are ruptures with relatively low dissimilarity and can fit the dominant trends of the Alaska slip inversion (Figures 10c and 10d). Both ruptures shown below experience three slip asperities in a

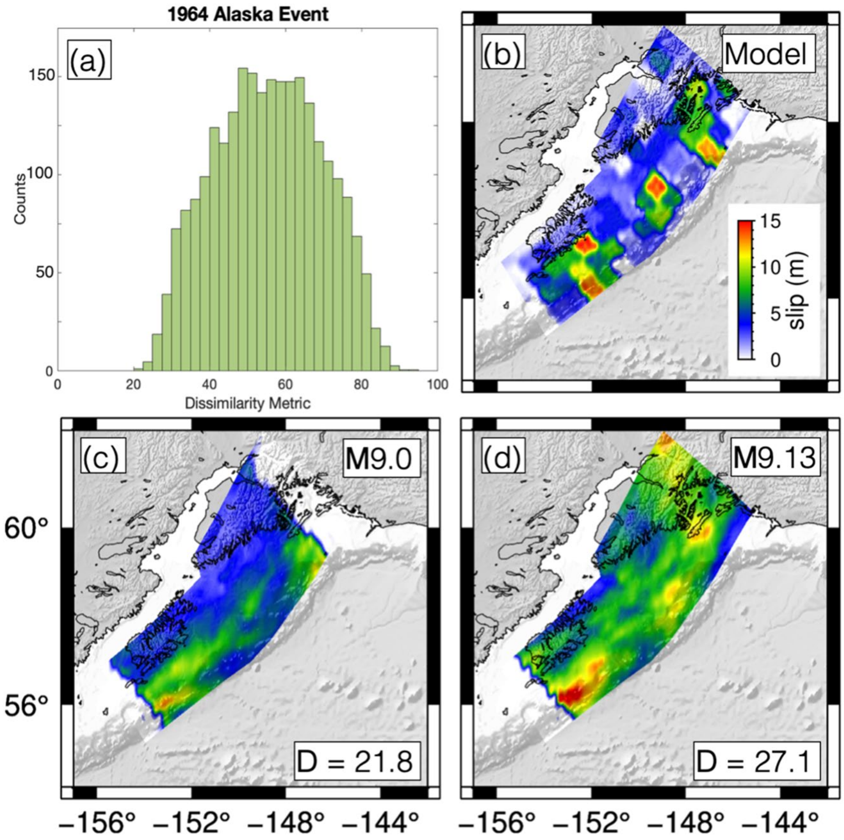

Figure 10. (a) Dissimilarity histogram distribution with a bin width of 2.5 for the 1964 Alaska event. (b) Slip model from Ichinose et al. (2007) that is used as the model we are trying to reproduce with the stochastic ruptures. (c) Example **M**9.0 rupture that has the lowest dissimilarity compared to any other modeled rupture. Color is represented by slip in meters shown in (a). (d) Same as (c) but for a **M**9.13 rupture and a larger dissimilarity.

similar location to the Ichinose model, with slip between 10 and 15 m in each region. Figure 10d experience a greater degree and dispersion of large slip throughout the modeled region, but still matches the slip inversion decently.

While there are no ruptures that fall below the threshold we applied for the Tohoku event, we note that this is an imperfect qualifier potentially specific for Japan. Several ruptures for the Alaska event both matched the slip asperity location and peak slip relatively well, with relatively small dissimilarity values. We still consider the stochastic approach used here to successfully reproduce the dominant trends associated with the Ichinose slip pattern for some example synthetic ruptures as seen by Figure 10.

4. Discussion

It is worth repeating here the intent of our study. We are focused on using these past large ruptures to validate the VK ACF method for stochastic slip rupture modeling. With few and rather general constraints applied to the method, we want to validate that this method can produce realistic large ruptures. Importantly, the ruptures are all completely blind to the inversion they are being compared to. The ability of this stochastic approach to produce ruptures at different subduction zones that match these historic earthquakes will provide weight and a measure of validation that the technique may be used for future studies globally. We note, however, that there is still uncertainty in the "full stack" of a PTHA calculation.

Assessing and determining an appropriate numeric qualifier for reproducing past ruptures is difficult. For the Tohoku case, we utilize three metrics to quantify a rupture's likeness to the past event: one based on direct slip pattern dissimilarity and two based on inundation analyses. Still, there is considerable uncertainty in the ability to assess likeness between the synthetic ruptures and the event. All metrics used in this study have strengths and weaknesses associated with their results. For instance, inundation percentage is a simple binary metric that is more forgiving of the uncertainties in inundation modeling than other statistical errors would be. Since the percentage only records whether a point is wetted or not, a rupture can grossly over inundate while producing a high inundation percentage. Luckily, for the Tohoku case, we are assessing rupture similarity using three metrics in total (dissimilarity, RMSE, and inundation percentage). Still however, the three metrics presented here are not perfect indicators. We are also limited in this study by the distribution of survey locations following the 2011 tsunami. The inundation points recorded throughout Japan are not equally distributed, but rather are more densely concentrated along the Sanriku Coast and Sendai Bay where the largest concentration of points are present. This may in turn create a bias in the final RMSE even though these is only a small region effected. Even though there are associated errors and shortcomings with the tsunami metrics, utilizing them in conjunction with the dissimilarity metric provides a greater sense of rupture likeness.

For all 330 ruptures, the RMSE of inundation has a minimum just below 7 m and a maximum just over 10 m. Regardless of rupture class, the Sanriku coast (between 38°N and 39°N) has the largest discrepancies between the model and survey. This region also experienced the largest coastal inundation following the 2011 earthquake, with some areas reaching almost 40 m in amplitude (Figure 4). Inundation residuals between modeled points and surveyed points have the largest values in the Sanriku coastal region. Unsurprisingly, if we look at residuals based on distance from the coast, we observe on average the further the inundation point was recorded, the smaller the residual is for all rupture classes (Figures 6c and 6f). Since the Sanriku coast region is misrepresented more often than other regions, there a general RMSE signal that is contained in all results. This may in turn lead to a range of RMSE values that seem confined in distribution.

It should also be recognized that calculating inundation on land is a complex process. The method for modeling inundation here uses a bare Earth digital elevation model that excludes alterations to topography including vegetation, buildings, and roads which all influence the onshore wave propagation. Similarly, we only model topography and bathymetry to the finest level of 3 arcseconds, or around 90 m resolution. This is fine for offshore wave propagation modeling, however, for terrestrial wave modeling this could still be considered coarse and lead to uncertainties in the resulting inundations. Although we can model topography to 1 arcsecond, the domain used here is so large we are unable to include that level of resolution in elevation data into the workflow. Melgar and Bock (2015) measured the terrain ruggedness index (TRI) along the Japan coast using a 3 arcsecond elevation model. The TRI determines the mean difference between elevation at one pixel and its neighboring pixels. Here they observe that the Sanriku coast has the highest values of TRI and the most instances of non-wetted inundation points by the simulations. This is similarly experienced by all our models. Yet even with the uncertainties of the inundation modeling, we can fit the tsunami inundation percentage data with over 80% for ruptures with relatively low dissimilarity values.

The four recorded earthquakes chosen for this study are all **M**9+ events that are characterized by a unique coseismic slip characteristics. Based on the Minson model, the 2011 Tohoku rupture experienced near-trench slip over 70 m, which had not been seen prior and was thought to be highly unlikely. The 1960 Chile event is the largest earthquake that has occurred during instrumental times, with three large slip asperities throughout the rupture area. The 2004 Sumatra event ruptured a portion of the Sumatra-Andaman subduction zone over 1,300 km long, a length that has never been observed before. Although there have been five **M**9+ earthquakes since the use of seismic monitoring, we omit the 1952 Kamchatka **M**9.0 event. To our knowledge, while there are some geologic observations of the resulting tsunami (e.g., MacInnes et al., 2010), given the sparsity of geophysical data at the time, there is no heterogenous slip inversion that can be used as basis for comparison.

From analysis of modeling of these events, we can conclude that the stochastic modeling approach can, at least to first order, reproduce realistic ruptures for all the four events we observed, without using coupling as an a priori constraint. We note that the Alaska event had the poorest distribution of dissimilarity values out of the four ruptures. For this case, ruptures did not fall below the dissimilarity threshold set from the Tohoku case. Yet as we said before, this "threshold" is arbitrary and should not be used in full faith for other subduction zones. There are Alaska stochastic ruptures that have relatively low dissimilarity and contain the dominant slip characteristics seen in the example slip model. Because of this, we do still consider this approach applicable at reproducing that event.

Throughout all four cases, we did not vary the input statistics or assumptions for any rupture, besides potential coupling constraints or rupture domain geometry. Similarly, the four earthquakes used in this study all follow the scaling law from Blaser et al. (2010) within 2σ uncertainty for both fault length and width. Both the Alaska and the Japan events fall below 1σ as well as one of the two dimensions for the Sumatra and Chile events.

So, the earthquakes used in this study are well accounted for based on the empirical scaling law from Blaser et al. (2010). While maintaining generic statistics derived from worldwide events (e.g., Goda et al., 2016; Melgar & Hayes, 2019), we can reproduce any of the **M**9+ ruptures relatively well. With this in consideration, the stochastic slip modeling approach does have the capability to represent large magnitude ruptures.

In Melgar and Hayes (2019), an updated value for the Hurst exponent was determined as preferable (0.4 rather than 0.75 from Mai & Beroza, 2002). While we used the older value for the Hurst exponent, we tested the impact this might have on the results mentioned prior by running models for the homogeneous case for the Japan Trench. We then computed the ruptures' dissimilarity to the Minson model and found that applying the updated Hurst exponent did not impact the results and the observed distribution of dissimilarity values is comparable to the ones mentioned prior. So, while it may be more applicable to run the VK stochastic method with the updated Hurst exponent, for this study we find that either one produces similar results.

Although for the four events we can produce stochastic models with low dissimilarity values ($D = 15$–20), we could not reproduce the slip distributions with identical or lower dissimilarity values. One way we could determine whether the VK ACF holds valid for these ruptures is by comparing the slip pattern spectra with the power law VK ACF distribution. This will be the subject for future work. There is a potential that changing some of the parameters used could decrease the dissimilarity values, however, as stated above, altering the Hurst exponent had little influence. The correlation lengths used in this study have been shown to fit for the 2010 Maule **M**8.8 and the 2011 Tohoku events (Melgar & Hayes, 2019). This is not to say that the potential for changing the parameters might contribute to better fits to the slip models but may need to be explored more in future work. Still, we consider the best fit adequate for our study for assessing the applicability of using the VK stochastic method for modeling great earthquakes.

We note here that while we studied four of the five **M**9+ ruptures in instrumental time, we only focused on a singular slip inversion for each as the representative model we attempted to reproduce using stochastic modeling. For some of these ruptures, there were several other available slip models that we could have used. We provide several reasons that justify our decision for each rupture. For instance, all slip inversions used here share similar slip patterns with most other inversions for their given ruptures. Calculating dissimilarity between these stochastic models and other slip inversions for the same ruptures would not vary substantially given the large similarities between inversions and the dissimilarity metric's increase weight on high slip patches.

Small and Melgar (2021) argued that including coupling to inform slip in the stochastic workflow has the potential to impact the technique's ability to create realistic ruptures. The analyses shown here argue that this can be true. The trench-locking class of Tohoku ruptures produces a greater percentage of ruptures below the dissimilarity threshold and generally leads to a tsunami inundation pattern that more closely replicates what was seen in the post-event survey. Compared to the homogeneous class, the trench-locking class has a probability of creating a "Tohoku-like" rupture that is four times more likely (57 total ruptures compared to 14 in the homogeneous class). Meanwhile for the trench-creeping class, no ruptures below the desired threshold are produced. This can be interpreted as the trench-creeping class has less ability to produce realistic ruptures. While including the "correct" coupling model has generally positive effects, including the "wrong" model can have very negative effects as well. So, a key finding in this work is that unless coupling is known with some certainty, for example, because it was obtained by including offshore geodetic measurements, it is safer to assume a homogenous distribution. We will note here that the nature is coupling is not fully understood. We assume here a simple relationship between slip potential and coupling ratio. If we include other fault zone characteristics like frictional stability, regions of stable sliding may potentially contribute in slip (Kozdon & Dunham, 2013); however, more is needed to be done to include such potentials in this method.

The drastic difference in the results of the two coupling models highlights the fundamental difference between them and the key characteristic of the Minson model. The 2011 Tohoku-Oki rupture was surprising when it first occurred because of the presence of large slip (~60–80 m) in the shallowest portion of the megathrust (Lay, 2018) (Figure 2a). In this model, the large slip asperity occurs below 20 km in depth, with slip occurring up to the trench. The presence of shallow slip here is directly in contrast to the fundamental assumption of the trench-creeping class. Another direct result of the trench-creeping pattern of coupling is apparent in the tsunami inundation results. At intermediate dissimilarity values (35–50), the trench-creeping class has more accurate inundation results than the other two classes at the same dissimilarity values (Figure 7). For dissimilarity values where the other classes have inundation percentages less than 80%, most of the trench-creeping ruptures are greater than

80% inundated. This discrepancy is due to the location of dominant slip for the trench-creeping class ruptures. The region of largest slip deficit rate is present directly offshore of the Miyagi Prefecture along the Sanriku Coast (38.2°N). Because of this, the megathrust in this region typically has the largest slip in the hypothetical ruptures. Although slip occurring here is at depths greater than 25 km, its proximity to the coast with enough amplitude can still create devastating tsunamis. So, even though a given rupture for the trench-creeping class has a larger dissimilarity value, it may still produce tsunami amplitudes that are similar to those of the real rupture.

The trench-locking class, on the other hand, is defined by a coupling pattern that correlates well with the Minson model. The trench-locking class has SDR accumulating all along the Japan Trench, with over 40 mm/yr of slip accumulation occurring in the same location as the dominant slip patch in the Minson model. Since there are high SDR rates that correlate with areas of high slip in the Minson model, these areas will have a greater probability of producing higher slip in the calculated rupture models. When we are modeling ruptures, if the correct rupture geometry and magnitude are picked from the scaling laws, the trench-locking class will have the highest probability of reproducing the ruptures.

By adding the right coupling model, we can more likely produce "Tohoku-like" or realistic ruptures. This can be very helpful for future hazard studies in that we may be able to better produce realistic ruptures by including a model for coupling. However, as we have seen, the impact of choosing one model over the other produces drastically different results. Determining which coupling model is more accurate is a difficult problem as it will require extensive seafloor instrumentation (e.g., Yokota et al., 2016). Luckily, the homogeneous class which does not utilize the coupling pattern still produces realistic ruptures as seen by all three of the example global earthquakes we calculated dissimilarity for. Although this produced fewer ruptures under the dissimilarity threshold than the trench-coupling class, it still has the capability to reproduce the slip models. So, rather than potentially misrepresenting the pattern of coupling, it is best to utilize the homogeneous method for stochastic modeling unless there is more certainty in the pattern of coupling.

Finally, we note that there is still uncertainty regarding the "full stack" of a PTHA calculation. The work here is related to that fundamental question of the applicability of the stochastic method for use in hazard related studies. We make a point that this method can produce realistic large ruptures that match reasonably well past observed historic events given the general statistical assumptions. Similarly, there is potential that applying a coupling constrained background slip model in the workflow may produce better fits to the historic ruptures. But this work presented here does not provide insight on whether the method will accurately replicate future yet to occur ruptures. Subduction zones are complex systems with seismic cycles of centurial to millennial time scales which we've only observed for a limited time. The issue of whether stochastic slip can or should be deployed for a PTHA (or PSHA) calculation, given this uncertainty, remains one worthy of debate. Here, we argue that the fact that it can replicate past ruptures suggests that it should play an important role.

5. Conclusion

We tested whether the slip distributions calculated using stochastic slip rupture modeling are "realistic" by attempting to reproduce slip distributions that match what is seen in **M**9+ events recorded in instrumental time. We first started with the 2011 **M**9.1 Tohoku-Oki earthquake and tsunami where we assessed both a stochastic method with a homogeneous background mean model and an interseismic coupling constrained stochastic method. We quantified the dissimilarity of slip distribution between the modeled ruptures and a slip inversion for the event. In addition to the slip pattern, we modeled high resolution tsunami inundation for 330 ruptures and compared the results to an inundation survey along the eastern coastline of Japan. We found that both the homogeneous and trench-locking classes could reproduce the 2011 Tohoku-Oki slip distribution defined by the Minson model and could model tsunami inundation results matching the post-earthquake tsunami survey. The trench-creeping class, however, could not produce any ruptures that qualified as "Tohoku-like," highlighting the varying effect a coupling constraint holds on the stochastic methodology. Because of the variable influence that either coupling model has on the output ruptures, we note that without strong reason to favor one coupling model over another, coupling should be excluded from the stochastic slip process to not introduce inaccurate biases. We also showed that for other great earthquakes such as the 1960 **M**9.4–9.6 Chile, 1964 **M**9.2 Alaska, and 2004 **M**9.1–9.3 Sumatra stochastic slip modeling has the capability to produce realistic ruptures. So, although the trench-locking class outperformed the homogeneous class for the Tohoku earthquake, all three earthquakes studied here were able to be reproduced using the homogeneous background slip method for stochastic slip modeling. Though we cannot say the stochastic method can perfectly represent subduction zone earthquake slip statistics, we add confidence in this approach's ability to reproduce realistic large magnitude ruptures. To end, we note that by increasing seafloor GNSS instrumentation at subduction zones, we may remedy the uncertainty of the coupling patterns in the shallow most portions of subduction zones so we can utilize the coupling constraint more confidently in future studies.

Data Availability Statement

All synthetic ruptures for the four rupture groups (Tohoku, Chile, Sumatra, and Alaska) are available for download on zenodo (Small & Melgar, 2023).

Acknowledgments
This work was funded by NSF Graduate Research Fellowship Program Grant NSF16104 and NSF Grant OAC-1835661. Partial support is also from the NASA Grants 80NSSC19K1104, 80NSSC19K0360, and 80NSSC22K0458.

References

Ammon, C. J., Ji, C., Thio, H. K., Robinson, D., Ni, S., Hjorleifsdottir, V., et al. (2005). Rupture process of the 2004 Sumatra-Andaman earthquake. *Science*, *308*(5725), 1133–1139. https://doi.org/10.1126/science.1112260

Ammon, C. J., Lay, T., Kanamori, H., & Cleveland, M. (2011). A rupture model of the 2011 off the Pacific coast of Tohoku Earthquake. *Earth Planets and Space*, *63*(7), 693–696. https://doi.org/10.5047/eps.2011.05.015

Barnhart, W. D., Murray, J. R., Briggs, R. W., Gomez, F., Miles, C. P., Svarc, J., et al. (2016). Coseismic slip and early afterslip of the 2015 Illapel, Chile, earthquake: Implications for frictional heterogeneity and coastal uplift. *Journal of Geophysical Research: Solid Earth*, *121*(8), 6172–6191. https://doi.org/10.1002/2016jb013124

Blaser, L., Krüger, F., Ohrnberger, M., & Scherbaum, F. (2010). Scaling relations of earthquake source parameter estimates with special focus on subduction environment. *Bulletin of the Seismological Society of America*, *100*(6), 2914–2926. https://doi.org/10.1785/0120100111

Bletery, Q., Sladen, A., Jiang, J., & Simons, M. (2016). A Bayesian source model for the 2004 great Sumatra-Andaman earthquake. *Journal of Geophysical Research: Solid Earth*, *121*(7), 5116–5135. https://doi.org/10.1002/2016jb012911

Comninou, M., & Dundurs, J. (1975). The angular dislocation in a half space. *Journal of Elasticity*, *5*(3), 203–216. https://doi.org/10.1007/bf00126985

Davies, G. (2019). Tsunami variability from uncalibrated stochastic earthquake models: Tests against deep ocean observations 2006–2016. *Geophysical Journal International*, *218*(3), 1939–1960. https://doi.org/10.1093/gji/ggz260

Davies, G., Horspool, N., & Miller, V. (2015). Tsunami inundation from heterogeneous earthquake slip distributions: Evaluation of synthetic source models. *Journal of Geophysical Research: Solid Earth*, *120*(9), 6431–6451. https://doi.org/10.1002/2015jb012272

Frankel, A., Wirth, E., Marafi, N., Vidale, J., & Stephenson, W. (2018). Broadband synthetic seismograms for magnitude 9 earthquakes on the Cascadia megathrust based on 3D simulations and stochastic synthetics, Part 1: Methodology and overall results methodology and overall results. *Bulletin of the Seismological Society of America*, *108*(5A), 2347–2369. https://doi.org/10.1785/0120180034

Geist, E. L., Titov, V. V., Arcas, D., Pollitz, F. F., & Bilek, S. L. (2007). Implications of the 26 December 2004 Sumatra–Andaman earthquake on tsunami forecast and assessment models for great subduction-zone earthquakes. *Bulletin of the Seismological Society of America*, *97*(1A), S249–S270. https://doi.org/10.1785/0120050619

Geuzaine, C., & Remacle, J. F. (2009). Gmsh: A 3-D finite element mesh generator with built-in pre-and post-processing facilities. *International Journal for Numerical Methods in Engineering*, *79*(11), 1309–1331. https://doi.org/10.1002/nme.2579

Goda, K., Yasuda, T., Mori, N., & Mai, P. M. (2015). Variability of tsunami inundation footprints considering stochastic scenarios based on a single rupture model: Application to the 2011 Tohoku earthquake. *Journal of Geophysical Research: Oceans*, *120*(6), 4552–4575. https://doi.org/10.1002/2014jc010626

Goda, K., Yasuda, T., Mori, N., & Maruyama, T. (2016). New scaling relationships of earthquake source parameters for stochastic tsunami simulation. *Coastal Engineering Journal*, *58*(3), 1650010-1–1650010-40. https://doi.org/10.1142/s0578563416500108

Gopinathan, D., Venugopal, M., Roy, D., Rajendran, K., Guillas, S., & Dias, F. (2017). Uncertainties in the 2004 Sumatra–Andaman source through nonlinear stochastic inversion of tsunami waves. *Proceedings of the Royal Society A: Mathematical, Physical & Engineering Sciences*, *473*(2205), 20170353. https://doi.org/10.1098/rspa.2017.0353

Graves, R., Jordan, T. H., Callaghan, S., Deelman, E., Field, E., Juve, G., et al. (2011). CyberShake: A physics-based seismic hazard model for southern California. *Pure and Applied Geophysics*, *168*(3), 367–381. https://doi.org/10.1007/s00024-010-0161-6

Gregor, N. J., Silva, W. J., Wong, I. G., & Youngs, R. R. (2002). Ground-motion attenuation relationships for Cascadia subduction zone megathrust earthquakes based on a stochastic finite-fault model. *Bulletin of the Seismological Society of America*, *92*(5), 1923–1932. https://doi.org/10.1785/0120000260

Gudmundsson, Ó., & Sambridge, M. (1998). A regionalized upper mantle (RUM) seismic model. *Journal of Geophysical Research*, *103*(B4), 7121–7136. https://doi.org/10.1029/97jb02488

Hayes, G. P., Moore, G. L., Portner, D. E., Hearne, M., Flamme, H., Furtney, M., & Smoczyk, G. M. (2018). Slab2, a comprehensive subduction zone geometry model. *Science*, *362*(6410), 58–61. https://doi.org/10.1126/science.aat4723

Herrero, A., & Bernard, P. (1994). A kinematic self-similar rupture process for earthquakes. *Bulletin of the Seismological Society of America*, *84*(4), 1216–1228. https://doi.org/10.1785/bssa0840041216

Ho, T. C., Satake, K., Watada, S., & Fujii, Y. (2019). Source estimate for the 1960 Chile earthquake from joint inversion of geodetic and transoceanic tsunami data. *Journal of Geophysical Research: Solid Earth*, *124*(3), 2812–2828. https://doi.org/10.1029/2018jb016996

Ichinose, G., Somerville, P., Thio, H. K., Graves, R., & O'Connell, D. (2007). Rupture process of the 1964 Prince William Sound, Alaska, earthquake from the combined inversion of seismic, tsunami, and geodetic data. *Journal of Geophysical Research*, *112*(B7), B07306. https://doi.org/10.1029/2006jb004728

Ide, S., Baltay, A., & Beroza, G. C. (2011). Shallow dynamic overshoot and energetic deep rupture in the 2011 M w 9.0 Tohoku-Oki earthquake. *Science*, *332*(6036), 1426–1429. https://doi.org/10.1126/science.1207020

Ji, C. (2005). Preliminary rupture model for the December 26, 2004 earthquake, off the west coast of Northern Sumatra, magnitude 9.1.

Konca, A. O., Avouac, J. P., Sladen, A., Meltzner, A. J., Sieh, K., Fang, P., et al. (2008). Partial rupture of a locked patch of the Sumatra megathrust during the 2007 earthquake sequence. *Nature*, *456*(7222), 631–635. https://doi.org/10.1038/nature07572

Kozdon, J. E., & Dunham, E. M. (2013). Rupture to the trench: Dynamic rupture simulations of the 11 March 2011 Tohoku Earthquake. *Bulletin of the Seismological Society of America*, *103*(2B), 1275–1289. https://doi.org/10.1785/0120120136

Kragh, E. D., & Christie, P. (2002). Seismic repeatability, normalized rms, and predictability. *The Leading Edge*, *21*(7), 640–647. https://doi.org/10.1190/1.1497316

Lavallée, D., & Archuleta, R. J. (2003). Stochastic modeling of slip spatial complexities for the 1979 Imperial Valley, California, earthquake. *Geophysical Research Letters*, *30*(5), 1245. https://doi.org/10.1029/2002gl015839

Lay, T. (2018). A review of the rupture characteristics of the 2011 Tohoku-Oki Mw 9.1 earthquake. *Tectonophysics*, *733*, 4–36. https://doi.org/10.1016/j.tecto.2017.09.022

LeVeque, R. J., George, D. L., & Berger, M. J. (2011). Tsunami modelling with adaptively refined finite volume methods. *Acta Numerica*, *20*, 211–289. https://doi.org/10.1017/s0962492911000043

LeVeque, R. J., Waagan, K., González, F. I., Rim, D., & Lin, G. (2016). Generating random earthquake events for probabilistic tsunami hazard assessment. In *Global tsunami science: Past and future, volume I* (pp. 3671–3692). Birkhäuser.

Li, S., & Freymueller, J. T. (2018). Spatial variation of slip behavior beneath the Alaska Peninsula along Alaska-Aleutian subduction zone. *Geophysical Research Letters*, *45*(8), 3453–3460. https://doi.org/10.1002/2017gl076761

Lin, J. T., Melgar, D., Thomas, A. M., & Searcy, J. (2021). Early warning for great earthquakes from characterization of crustal deformation patterns with deep learning. *Journal of Geophysical Research: Solid Earth*, *126*(10), e2021JB022703. https://doi.org/10.1029/2021jb022703

Lindsey, E. O., Mallick, R., Hubbard, J. A., Bradley, K. E., Almeida, R. V., Moore, J. D., et al. (2021). Slip rate deficit and earthquake potential on shallow megathrusts. *Nature Geoscience*, *14*(5), 321–326. https://doi.org/10.1038/s41561-021-00736-x

Loveless, J. P., & Meade, B. J. (2015). Kinematic barrier constraints on the magnitudes of additional great earthquakes off the East Coast of Japan. *Seismological Research Letters*, *86*(1), 202–209. https://doi.org/10.1785/0220140083

Loveless, J. P., & Meade, B. J. (2016). Two decades of spatiotemporal variations in subduction zone coupling offshore Japan. *Earth and Planetary Science Letters*, *436*, 19–30. https://doi.org/10.1016/j.epsl.2015.12.033

MacInnes, B. T., Weiss, R., Bourgeois, J., & Pinegina, T. K. (2010). Slip distribution of the 1952 Kamchatka great earthquake based on near-field tsunami deposits and historical records. *Bulletin of the Seismological Society of America*, *100*(4), 1695–1709. https://doi.org/10.1785/0120090376

Mai, P. M., & Beroza, G. C. (2002). A spatial random field model to characterize complexity in earthquake slip. *Journal of Geophysical Research*, *107*(B11), ESE-10-1–ESE-10-21. https://doi.org/10.1029/2001jb000588

Meade, B. J., & Loveless, J. P. (2009). Block modeling with connected fault-network geometries and a linear elastic coupling estimator in spherical coordinates. *Bulletin of the Seismological Society of America*, *99*(6), 3124–3139. https://doi.org/10.1785/0120090088

Melgar, D., & Bock, Y. (2015). Kinematic earthquake source inversion and tsunami runup prediction with regional geophysical data. *Journal of Geophysical Research: Solid Earth*, *120*(5), 3324–3349. https://doi.org/10.1002/2014jb011832

Melgar, D., & Hayes, G. P. (2019). The correlation lengths and hypocentral positions of great earthquakes. *Bulletin of the Seismological Society of America*, *109*(6), 2582–2593. https://doi.org/10.1785/0120190164

Melgar, D., LeVeque, R. J., Dreger, D. S., & Allen, R. M. (2016). Kinematic rupture scenarios and synthetic displacement data: An example application to the Cascadia subduction zone. *Journal of Geophysical Research: Solid Earth*, *121*(9), 6658–6674. https://doi.org/10.1002/2016jb013314

Métois, M., Socquet, A., Vigny, C., Carrizo, D., Peyrat, S., Delorme, A., et al. (2013). Revisiting the North Chile seismic gap segmentation using GPS-derived interseismic coupling. *Geophysical Journal International*, *194*(3), 1283–1294. https://doi.org/10.1093/gji/ggt183

Minson, S. E., Simons, M., Beck, J. L., Ortega, F., Jiang, J., Owen, S. E., et al. (2014). Bayesian inversion for finite fault earthquake source models–II: The 2011 great Tohoku-Oki, Japan earthquake. *Geophysical Journal International*, *198*(2), 922–940. https://doi.org/10.1093/gji/ggu170

Moreno, M., Rosenau, M., & Oncken, O. (2010). 2010 Maule earthquake slip correlates with pre-seismic locking of Andean subduction zone. *Nature*, *467*(7312), 198–202. https://doi.org/10.1038/nature09349

Mori, N., Mai, P. M., Goda, K., & Yasuda, T. (2017). Tsunami inundation variability from stochastic rupture scenarios: Application to multiple inversions of the 2011 Tohoku, Japan earthquake. *Coastal Engineering*, *127*, 88–105. https://doi.org/10.1016/j.coastaleng.2017.06.013

Mori, N., Takahashi, T., & 2011 Tohoku Earthquake Tsunami Joint Survey Group (2012). Nationwide post event survey and analysis of the 2011 Tohoku earthquake tsunami. *Coastal Engineering Journal*, *54*(1), 1250001-1–1250001-27. https://doi.org/10.1142/s0578563412500015

Murphy, S., Scala, A., Herrero, A., Lorito, S., Festa, G., Trasatti, E., et al. (2016). Shallow slip amplification and enhanced tsunami hazard unravelled by dynamic simulations of mega-thrust earthquakes. *Scientific Reports*, *6*(1), 1–12. https://doi.org/10.1038/srep35007

Okada, Y. (1985). Surface deformation due to shear and tensile faults in a half-space. *Bulletin of the Seismological Society of America*, *75*(4), 1135–1154. https://doi.org/10.1785/bssa0750041135

Oleskevich, D. A., Hyndman, R. D., & Wang, K. (1999). The updip and downdip limits to great subduction earthquakes: Thermal and structural models of Cascadia, south Alaska, SW Japan, and Chile. *Journal of Geophysical Research*, *104*(B7), 14965–14991. https://doi.org/10.1029/1999jb900060

Perfettini, H., Avouac, J. P., Tavera, H., Kositsky, A., Nocquet, J. M., Bondoux, F., et al. (2010). Seismic and aseismic slip on the Central Peru megathrust. *Nature*, *465*(7294), 78–81. https://doi.org/10.1038/nature09062

Plafker, G. (1967). *Surface faults on Montague Island associated with the 1964 Alaska earthquake* (p. 42). US Government Printing Office.

Razafindrakoto, H. N., Mai, P. M., Genton, M. G., Zhang, L., & Thingbaijam, K. K. (2015). Quantifying variability in earthquake rupture models using multidimensional scaling: Application to the 2011 Tohoku earthquake. *Geophysical Journal International*, *202*(1), 17–40. https://doi.org/10.1093/gji/ggv088

Rhie, J., Dreger, D., Burgmann, R., & Romanowicz, B. (2007). Slip of the 2004 Sumatra–Andaman earthquake from joint inversion of long-period global seismic waveforms and GPS static offsets. *Bulletin of the Seismological Society of America*, *97*(1A), S115–S127. https://doi.org/10.1785/0120050620

Rodriguez, E. E., & Russo, R. M. (2020). Southern Chile crustal structure from teleseismic receiver functions: Responses to ridge subduction and terrane assembly of Patagonia. *Geosphere*, *16*(1), 378–391. https://doi.org/10.1130/ges01692.1

Ruhl, C. J., Melgar, D., Grapenthin, R., & Allen, R. M. (2017). The value of real-time GNSS to earthquake early warning. *Geophysical Research Letters*, *44*(16), 8311–8319. https://doi.org/10.1002/2017gl074502

Ruiz, J., Baumont, D., Bernard, P., & Berge-Thierry, C. (2007). New approach in the kinematic k−2 source model for generating physical slip velocity functions. *Geophysical Journal International*, *171*(2), 739–754. https://doi.org/10.1111/j.1365-246x.2007.03503.x

Scala, A., Lorito, S., Romano, F., Murphy, S., Selva, J., Basili, R., et al. (2020). Effect of shallow slip amplification uncertainty on probabilistic tsunami hazard analysis in subduction zones: Use of long-term balanced stochastic slip models. *Pure and Applied Geophysics*, *177*(3), 1497–1520. https://doi.org/10.1007/s00024-019-02260-x

Sepúlveda, I., Liu, P. L. F., & Grigoriu, M. (2019). Probabilistic tsunami hazard assessment in South China Sea with consideration of uncertain earthquake characteristics. *Journal of Geophysical Research: Solid Earth*, *124*(1), 658–688. https://doi.org/10.1029/2018jb016620

Shao, G., Li, X., Ji, C., & Maeda, T. (2011). Focal mechanism and slip history of the 2011 Mw 9.1 off the Pacific coast of Tohoku Earthquake, constrained with teleseismic body and surface waves. *Earth Planets and Space*, *63*(7), 559–564. https://doi.org/10.5047/eps.2011.06.028

Small, D. T., & Melgar, D. (2021). Geodetic coupling models as constraints on stochastic earthquake ruptures: An example application to PTHA in Cascadia. *Journal of Geophysical Research: Solid Earth*, *126*(7), e2020JB021149. https://doi.org/10.1029/2020jb021149

Small, D. T., & Melgar, D. (2023). Rupture files [Dataset]. Zenodo. https://doi.org/10.5281/ZENODO.7734845

Somerville, P., Irikura, K., Graves, R., Sawada, S., Wald, D., Abrahamson, N., et al. (1999). Characterizing crustal earthquake slip models for the prediction of strong ground motion. *Seismological Research Letters*, *70*(1), 59–80. https://doi.org/10.1785/gssrl.70.1.59

Suito, H., & Freymueller, J. T. (2009). A viscoelastic and afterslip postseismic deformation model for the 1964 Alaska earthquake. *Journal of Geophysical Research*, *114*(B11), B11404. https://doi.org/10.1029/2008jb005954

Tozer, B., Sandwell, D. T., Smith, W. H., Olson, C., Beale, J. R., & Wessel, P. (2019). Global bathymetry and topography at 15 arc sec: SRTM15+. *Earth and Space Science*, *6*(10), 1847–1864. https://doi.org/10.1029/2019ea000658

Villegas-Lanza, J. C., Chlieh, M., Cavalié, O., Tavera, H., Baby, P., Chire-Chira, J., & Nocquet, J. M. (2016). Active tectonics of Peru: Heterogeneous interseismic coupling along the Nazca megathrust, rigid motion of the Peruvian Sliver, and Subandean shortening accommodation. *Journal of Geophysical Research: Solid Earth*, *121*(10), 7371–7394. https://doi.org/10.1002/2016jb013080

Wang, K., & Tréhu, A. M. (2016). Invited review paper: Some outstanding issues in the study of great megathrust earthquakes—The Cascadia example. *Journal of Geodynamics*, *98*, 1–18. https://doi.org/10.1016/j.jog.2016.03.010

Wei, S., Graves, R., Helmberger, D., Avouac, J. P., & Jiang, J. (2012). Sources of shaking and flooding during the Tohoku-Oki earthquake: A mixture of rupture styles. *Earth and Planetary Science Letters*, *333*, 91–100. https://doi.org/10.1016/j.epsl.2012.04.006

Wei, S., Sladen, A., & The ARIA Group (Caltech-JPL). (2011). Updated result 3/11/2011 (Mw 9.0), Tohoku-Oki, Japan. Source models of large earthquakes. Retrieved from http://www.tectonics.caltech.edu/slip_history/2011_taiheiyo-oki/index.html

Williamson, A., Melgar, D., & Rim, D. (2019). The effect of earthquake kinematics on tsunami propagation. *Journal of Geophysical Research: Solid Earth*, *124*(11), 11639–11650. https://doi.org/10.1029/2019jb017522

Wilson, D. L., Baddeley, A. J., & Owens, R. A. (1997). A new metric for grey-scale image comparison. *International Journal of Computer Vision*, *24*(1), 5–17. https://doi.org/10.1023/a:1007978107063

Yagi, Y., & Fukahata, Y. (2011). Rupture process of the 2011 Tohoku-Oki earthquake and absolute elastic strain release. *Geophysical Research Letters*, *38*(19), L19307. https://doi.org/10.1029/2011gl048701

Yamazaki, Y., Lay, T., Cheung, K. F., Yue, H., & Kanamori, H. (2011). Modeling near-field tsunami observations to improve finite-fault slip models for the 11 March 2011 Tohoku earthquake. *Geophysical Research Letters*, *38*(7), L00G15. https://doi.org/10.1029/2011gl049130

Yokota, Y., Ishikawa, T., Watanabe, S. I., Tashiro, T., & Asada, A. (2016). Seafloor geodetic constraints on interplate coupling of the Nankai Trough megathrust zone. *Nature*, *534*(7607), 374–377. https://doi.org/10.1038/nature17632

Yue, H., & Lay, T. (2013). Source rupture models for the M w 9.0 2011 Tohoku earthquake from joint inversions of high-rate geodetic and seismic data. *Bulletin of the Seismological Society of America*, *103*(2B), 1242–1255. https://doi.org/10.1785/0120120119